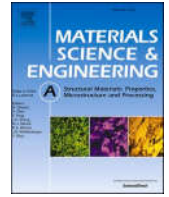


Contents lists available at ScienceDirect

Materials Science & Engineering A

journal homepage: www.elsevier.com/locate/msea

Influence of post-weld rolling and artificial aging on microstructure and mechanical properties of friction stir welded 2195-T4 Al-Li alloy joints

Peng Chen^{a,b,c,*}, Jie Wang^a, Ge Liu^d, Wenhao Chen^a, Yang Tang^e, Bensheng Huang^{a,**}, Zhiqing Zhang^{c,***}^a School of New Energy and Materials, Southwest Petroleum University, Chengdu, 610500, China^b Sichuan Provincial Engineering Research Center of Advanced Materials Manufacturing Technology for Shale Gas High-Efficient Exploitation, Southwest Petroleum University, Chengdu, 610500, China^c College of Materials Science and Engineering, Chongqing University, Chongqing, 400045, China^d School of Robot Engineering, Yangtze Normal University, Chongqing, 408100, China^e School of Mechatronic Engineering, Southwest Petroleum University, Chengdu, 610500, China

ARTICLE INFO

Keywords:

2195 Al-Li alloy
Friction stir welding
Post-welding heat treatment
Microstructure
Mechanical properties

ABSTRACT

Friction stir welding (FSW) of a naturally aged (T4) 2195 Al-Li alloy was conducted to study the effect of post-weld artificial aging (AA) and rolling + artificial aging (R + AA) on microstructure and mechanical properties of the FSW joints. Grain features were analyzed by electron back scattered diffraction (EBSD) technology, and precipitates were characterized using transmission electron microscopy (TEM) along [011]_{Al} and [001]_{Al} zone axes. Mechanical properties of the joints were evaluated through micro-hardness and tensile testing. The results indicate that grain development, including grain orientation, grain boundary components and dislocation density, varies within different regions of the As-welded joints due to complicated thermal-mechanical history. The alloying elements mostly exist as Guinier-Preston zones in the base material (BM) with a few formations of δ'/β' , and slightly precipitate into T_1 in the heat affected zone (HAZ), form σ in the thermal-mechanical affected zone (TMAZ), as well as develop T_1 and S' in the nugget zone (NZ) after FSW. The lowest hardness zone (LHZ) exhibits elevated precipitation levels, generating coarse T_1 and grain boundary precipitates with evident σ and precipitate free zone. The overall precipitation level of the As-welded joints remains minor, resulting in a slight decrease in hardness at the LHZ. Post-weld AA promotes many T_1 formations, enhancing the joint strength and hardness. As a result, the ultimate tensile strength (UTS) of the joints increases from 440 MPa to 506.5 MPa, while the elongation decreases from 13.5 % to 3.4 %. Furthermore, hardness profiles transform from a low-amplitude wave curve to a high-amplitude W-shaped curve, generating a significant LHZ due to the minimal precipitation of T_1 . Pre-rolling deformation can enhance dislocation density and low angle grain boundaries (LAGBs), promoting the nucleation of high-density, fine T_1 during artificial aging, and especially improves precipitation ability of the LHZ, leading to an elevated hardness increment in the region after AA. Compared to the Joint-AA, both strength and elongation of the Joint-R + AA increase, obtaining 530.5 MPa and 3.9 %, respectively.

1. Introduction

In recent years, the application of aluminum-lithium (Al-Li) alloys in the aerospace industry has garnered significant attention [1,2]. These alloys possess low density and high strength, presenting a compelling alternative for aerospace structures [3]. The successful use of Al-Li alloys is evident in the production of the fuselage, as well as the upper and

lower wings of the C919 large airplane [4]. The integration of these alloys resulted in a notable 7 % weight reduction for the aircraft, positively impacting its fuel consumption and performance via increased payload capability or longer endurance [4,5]. The usage of Al-Li alloy in aerospace vehicles serves as a symbol of the industry's commitment to adopting advanced materials and superior production techniques [5]. During the actual production, fabricating a large-scale Al-Li alloy

* Corresponding author. School of New Energy and Materials, Southwest Petroleum University, Chengdu, 610500, China.

** Corresponding author. School of New Energy and Materials, Southwest Petroleum University, Chengdu, 610500, China.

*** Corresponding author. College of Materials Science and Engineering, Chongqing University, Chongqing, 400045, China.

E-mail addresses: xd_chenpeng@163.com (P. Chen), hbslxp@163.com (B. Huang), zqzhang@cqu.edu.cn (Z. Zhang).<https://doi.org/10.1016/j.msea.2024.147165>

Received 28 February 2024; Received in revised form 14 August 2024; Accepted 22 August 2024

Available online 24 August 2024

0921-5093/© 2024 Elsevier B.V. All rights are reserved, including those for text and data mining, AI training, and similar technologies.

structure has been an essential technological advancement, with efficient joining methodologies being a significant hurdle for this high-tensile Al alloy [6,7].

Friction stir welding (FSW), a solid-state joining method, employs heat produced by a rotating tool to soften materials and create a bond between the adjacent plates [8]. Unlike fusion welding, FSW operates at relatively low temperatures, typically ranging from 0.6 to 0.9 times the melting temperature [8]. This low-temperature process minimizes the risk of thermal distortion and associated defects, guaranteeing high-quality joints. Conventional fusion welding techniques often encounter challenges in preserving the favorable mechanical attributes of Al-Li alloy due to the limited ductility and fracture toughness of the joints. Nevertheless, FSW has exhibited promising results in mitigating this degradation and creating dependable joints with improved mechanical properties. Consequently, it is recognized as an optimal method for welding of Al-Li alloys, with abundant related research ongoing [6–11].

Most works have concentration on optimizing process parameters, analyzing microstructural evolution, and evaluating the mechanical properties of the FSW joints [2]. By understanding the relationship between FSW parameters and the quality of Al-Li alloy FSW joints, investigators aim to enhance joint efficiency. Therefore, welding parameters for Al-Li alloys with varying chemical composition and plate thickness have been defined, illustrating notably enhanced joint performance [6]. To further increase the performance of Al-Li alloy FSW joints, novel FSW techniques, including dual-rotation friction stir welding (DR-FSW), stationary shoulder friction stir welding (SS-FSW) and ultrasound assisted friction stir welding (UA-FSW), have been researched [12–14]. As a result, joint strength of Al-Li alloy FSW has been dramatically improved, exhibiting an ultimate tensile strength (UTS) exceeding 490 MPa [10]. However, compared to the UTS of the base material (BM), the obtained maximum joint strength remains lower, failing to exploit the alloy's superior strength features. Further efforts are required to augment the mechanical properties of the joints.

Al-Li alloy belongs to precipitation-hardened Al alloys, which mechanical properties predominantly depend on precipitates. Hence, appropriate control over precipitate type, size and content can significantly enhance mechanical performance. As a representative of the widely used third-generation Al-Li alloys, 2195 Al-Li alloy has complex precipitate systems with numerous common precipitates. These precipitates undergo complicated evolution due to the sharp change FSW thermal-mechanical history in adjacent regions of the joints, usually including precipitate dissolution, precipitation, re-precipitation and coarsening [3,15,16]. Notably, T_1 (Al_2CuLi), the primary strengthening precipitate of Al-Cu-Li alloys, significantly influences its mechanical performance. As a result, the evolution of T_1 is extensively studied in FSW joints of 2195 Al-Li alloys [17–19]. Shen et al. [20] finds that numerous T_1 precipitates formed in the BM dissolve in the nugget zone (NZ) and thermal-mechanically affected zone (TMAZ), coarsen in the heat affected zone (HAZ), and lead to reduced joint strength. However, Chen et al. [21] reported that T_1 mostly dissolves in the TMAZ I, but coarsens in TMAZ II. Moreover, the researchers have shown that this precipitate is totally dissolved in the NZ and can re-form at the top of the NZ with high rotation speeds [22]. In summary, the dissolution, coarsening and precipitation of T_1 occur in the friction stir welded Al-Li alloy joints. Joint softening is mostly attributed to the dissolution and coarsening of this precipitate. Hence, the joint performance can be improved by adjusting T_1 formation. Numerous research indicates that reducing the heat input impact on T_1 through process parameter adjustments (predominantly rotational speed and welding speed) is effective, but difficult to achieve high-strength joints [11,15,23,24].

Post-welding heat treatment (PWHT) can enhance joint strength by controlling precipitate nucleation. It's often employed to raise the strength of Al-Li alloy fusion welded joints, while a little report exists for friction stir welded joints [25–27]. Vysotskiy et al. [28–32] has applied PWHT to 6xxx and 7xxx Al alloy FSW joints, significantly improving the

joint strength [30,32]. Their strategy is to promote the formation of numerous strengthening precipitates through post-weld solid solution (S) and artificial aging (AA). The specific heat treatment process is mainly related to the precipitation state of the BM. For the FSW joints where the BM is artificially aged (T6 and T8 status) or completely annealed (O status), S treatment is first conducted to completely dissolve the formed precipitate, followed by re-precipitating the strengthened precipitates as much as possible through AA treatment [31,33–35]. The joints with naturally aged (T4 status) base material, however, enhance strength with simple AA treatment alone. Generally, the AA treatment alone isn't as effective as S + AA treatment in enhancing joint strength. Nonetheless, the latter PWHT method is complex, and notably, grains of NZ can potentially grow abnormally during the S process, which could deteriorate joint toughness. Zhang et al. [11] performed S + AA treatment on the 2195-T8 Al-Li FSW joints, enhancing joint strength significantly by 30.1 %. However, due to the generation of abnormal grain growth (AGG) in the NZ, elongation of the joint after heat treatment is only 1.6 %. Therefore, finding the optimal PWHT process is crucial, and it is advised to avoid S treatment during the post-weld heat process. It is notable that the BM of the friction stir welded 2195 Al-Li alloy is mostly in T6 or T8 temper condition. This implies that to significantly strengthen the joint, S treatment cannot be avoided, unless given up the common precipitation states of the BM.

In the present work, naturally aged (T4 status) 2195 Al-Li alloy was adopted for FSW, and the joints were conducted to different post-weld AA treatment. The effect of the PWHT on microstructure and mechanical properties of the joint was discussed in detail. To this end, optical microscope (OM), electron back scattered diffraction (EBSD), scanning electron microscope (SEM) and transmission electron microscopy (TEM) were employed for microstructure characterization. Vickers hardness testers and universal testing machine were adopted to measure the hardness and tensile properties of the FSW joints.

2. Material and experimental work

In this research, 7.5 mm thick 2195-T4 Al-Li alloy plates underwent friction stir butt welding at a rotation speed of 700 rpm and a welding speed of 50 mm/min. Chemical compositions of the alloys were listed in Table 1. Welding direction (WD) was parallel to the rolling direction (RD) of the plates, using a shoulder plunge depth of 0.1 mm and a tool tilt angle of 2.5°. FSW tool is made of high-speed steel and consists of a concave shoulder with 18 mm in diameter and a threaded taper cylindrical pin of 6.9 mm in length. Post-welding heat treatment (PWHT), which took place after FSW, is detailed in Table 2, with designated abbreviations. Once PWHT was completed, microstructure characterization and mechanical property tests were performed. A visual guide to the experimental sequence can be found in Fig. 1.

Optical microscope (OM) observation was conducted on the transverse cross-section of the joints using the Zeiss Axiover 40 MAT. The specimens for OM observation were ground, polished, and carefully etched in Keller's reagents (2 ml hydrofluoric acid, 3 ml hydrochloric acid, 5 ml nitric acid and 190 ml water) at last. The EBSD specimens were prepared by grinding and mechanical polishing, and then electro-polishing with a mixture of 10 % $HClO_4$ and 90 % C_2H_5OH for 120 s at 20 V and $-20^\circ C$. EBSD test was carried out on a scanning electron microscope (SEM, Zeiss Auriga) with an operating voltage of 20 kV, with the EBSD scanning step size either 0.3 μm or 1 μm .

EBSD data was processed by HKL Channel 5 software. TEM samples were prepared via two methods: one was by twin-jet electro-polishing with a solution of 70 % CH_3OH and 30 % HNO_3 , applied at 15V and

Table 1
Chemical compositions of 2195-T4 Al-Li alloys (wt %).

| Cu | Li | Mg | Ag | Zr | Fe | Al |
|------|------|------|------|------|------|------|
| 4.00 | 1.00 | 0.44 | 0.40 | 0.11 | 0.05 | Bal. |

Table 2

Schemes of different treated joints.

| Designation | Heat treatment schemes |
|------------------|--|
| As-welded joints | / |
| Joints-AA | 160 °C artificial aging (AA) for 60 h |
| Joints-R + AA | 15 % rolling (R) deformation+160 °C artificial aging (AA) for 15 h |

–30 °C, and the other was by focused ion beam (FIB) technology using the Zeiss Auriga FIB-SEM.

TEM characterization was conducted via Thermo Scientific Talos F200S at 200 kV. Scanning transmission electron microscopy (STEM) and selected area electron diffraction (SAED) technologies were mainly used to explore precipitate features in different regions of the joints. Positions for TEM observation were marked with yellow points in Fig. 4.

MH-5L micro-hardness testers were used to measure hardness distribution across the joints' transverse cross-section, with an interval of 0.5 mm and a load of 500 g for 10 s, as shown in Fig. 1d. Tensile test samples were prepared following ASTM: E8- M11 guidelines, illustrated in Fig. 1e. Room-temperature tensile tests conducted with AG-X testing machines (maximum load of 50 kN, accuracy of $\pm 0.5\%$) at a displacement rate of 1 mm/min, with three samples per condition. Fracture morphology of the tensile test specimens was observed via Zeiss Auriga FIB-SEM.

3. Results

3.1. Hardness profile

Fig. 2 shows the microhardness distribution of the FSW joints, both before and after heat treatment. Prior to heat treatment, the joint hardness distribution fluctuates minimally, with an average hardness of approximately 130.4 HV. Notably, the hardness near the transition zone between the TMAZ and HAZ slightly decelerates, reaching a minimum of about 123.5 HV on the advancing side. Typically, the lowest hardness region (LHZ) in the FSW joint is quantified as a position with the lowest hardness. Post heat treatment, the joint hardness has increased, causing a significant fluctuation in the hardness distribution curve exhibiting a 'W' profile. Despite obtaining similar peak hardness values (>180 HV) across the BM, HAZ and NZ under the both heat treatment methods, there remain softening regions between the TMAZ and HAZ. Prior to and post heat treatment, position of the softening regions remains relatively consistent, with the Joints-AA attaining a minimum hardness value of approximately 137.2 HV (an increase of 11.1 %), while the Joints-R + AA produce an appreciably higher minimum hardness value, about 157.1 HV (an increase of 27.2 %).

3.2. Microstructure

3.2.1. Grain features

Fig. 3 shows inverse pole figure (IPF) of grains in different regions of the FSW joints prior to and post rolling deformation, in which different colors signify varying orientations within grains. The orientation-color card in the upper right in Fig. 3a depicts the reference for grain orientation and color, denoting red towards 100, green towards 101, and blue towards 111. It is evident that, in the As-welded FSW joints, the HAZ primarily consists of layered grains with strong 001 orientation (Fig. 3a), which closely resembles that of the BM (Figs. A-1a). Both the AS-TMAZ (Fig. 3b) and RS-TMAZ (Fig. 3d) are primarily composed of long, curving grains, and develop some fine recrystallization grains with random orientation. As compared with the AS-TMAZ, the RS-TMAZ possesses more substructures. The NZ is composed of fine, equiaxed recrystallization grains which are randomly orientated (Fig. 3c). After rolling deformation, grains in different regions of the joints sustain little morphological alterations. However, the uniformity of their inner color diminishes, signifying an increased internal grain misorientation. For example, a comparison of misorientation fluctuations in the grains of the HAZ before and after deformation is shown in Fig. 4, revealing a minimality misorientation fluctuation (less than 0.6°) before rolling, contrasted by a significant increase after rolling.

Fig. 5 shows the grain boundaries (GBs) distribution, the black lines indicating high angle grain boundaries (misorientation $\geq 15^\circ$), and the green lines signifying low angle grain boundaries

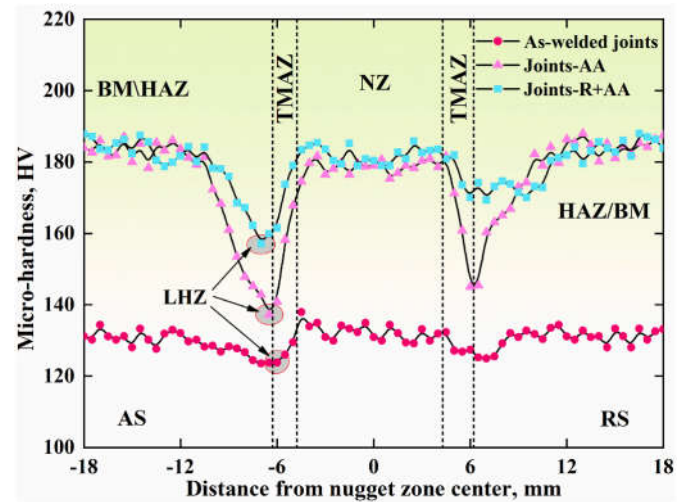


Fig. 2. Hardness distribution of the As-welded and PWHT joints.

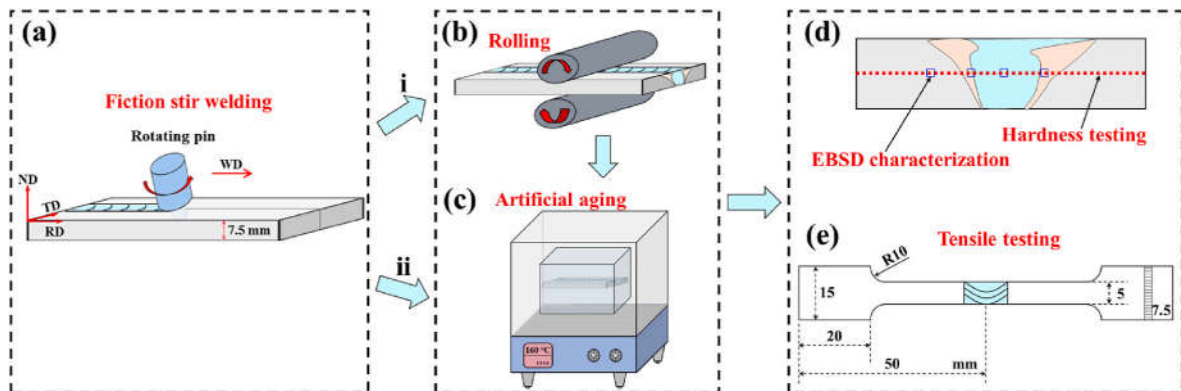


Fig. 1. Scheme of the experimental process including (a) friction stir welding, (b) rolling process, (c) artificial aging treatment, (d) EBSD characterization and hardness test and (e) tensile test samples.

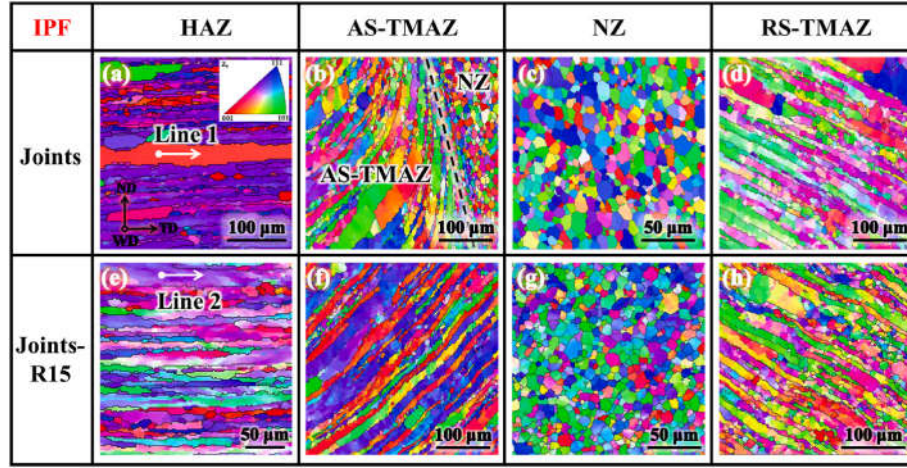


Fig. 3. IPF of the HAZ, AS-TMAZ, NZ and RS-TMAZ for (a–d) the As-welded joints and (e–h) the joints after rolling deformation.

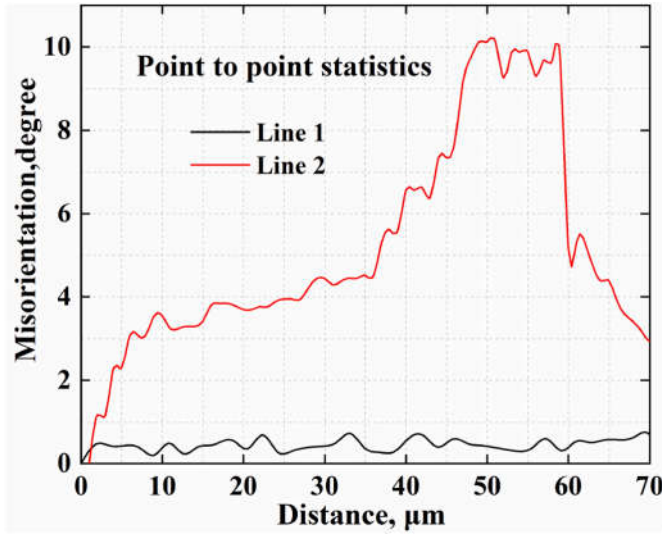


Fig. 4. Misorientation profile statistics in the HAZ of the Line 1 in Fig. 3a (As-welded joints) and Line 2 in Fig. 3e (Joints after rolling deformation).

($2^\circ \leq \text{misorientation} < 15^\circ$), in different regions of the FSW joints prior to and post rolling deformation. The corresponding GBs content statistics are presented in Fig. 6. Before deformation, in the HAZ, substructures mainly form in the elongated grains, and the wider elongated grains remain untainted by LAGBs. Moreover, the fraction of LAGBs is 50.9 %, and the HAGBs occupy 49.1 %. In the TMAZ, the elongated grains are interspersed with LAGBs resulting in numerous substructures (Fig. 5b). The fraction of LAGBs within the AS-TMAZ (39.4 %) is lesser compared to the RS-TMAZ (44.7 %). The minimum LAGBs generate in the NZ, about 15.6 %, and the fraction of HAGBs reaches 84.4 % (Fig. 6c). After rolling deformation, the proportion of LAGBs in the whole regions has increased, and the greatest increase occurs in the NZ. As a result, the content of LAGBs in the HAZ, AS-TMAZ, RS-TMAZ and NZ are 59.8 %, 52.1 %, 33.2 % and 56.2 %.

3.2.2. Precipitates

2195 Al-Li alloy presents intricate precipitation arrangements, comprising primarily Guinier-Preston zones (GPZs), T_1 (Al_2CuLi), θ' (Al_2Cu), δ' (Al_3Li), β' (Al_3Zr), S' (Al_2CuMg), and possibly σ ($\text{Al}_5\text{Cu}_6\text{Mg}$) as well [29]. When observed by TEM along different diffraction directions, these precipitates exhibit diverse morphologies and diffraction laws. Fig. 7 shows the schematic diagram of SAED patterns of the precipitates

along $[011]_{\text{Al}}$ and $[001]_{\text{Al}}$ zone axes. For precise identification, TEM analysis is focused on the diffraction patterns along $[011]_{\text{Al}}$ and $[001]_{\text{Al}}$ zone axes in this paper. Significantly, both δ' and β' share identical crystal structure (L1_2 structure) and morphology, developing into a composite precipitate of $\text{Al}_3(\text{Li}, \text{Zr})$. Hence, they are referred to δ'/β' in this study.

3.2.2.1. Precipitates in the NZ. Fig. 8 shows STEM-DF and SAED images of the NZ in the As-welded joints, Joints-AA and Joints-R + AA. Size distribution of T_1 in the NZ of the Joints-AA and Joints-R + AA are shown in Fig. 9.

In the NZ of the As-welded joints, a few needle-shaped precipitates with a length about 30–100 nm are identified as T_1 precipitates (Fig. 8a), which have an included angles 70.4° between the two variants and parallel to $[111]_{\text{Al}}$ direction. Spherical-like δ'/β' precipitates, evident in the STEM-DF images (Fig. 8a and d) along $[011]_{\text{Al}}$ and $[001]_{\text{Al}}$ zone axes, can be distinguished by their morphology and the diffraction spots at $1/2[002]_{\text{Al}}$ and $1/2[022]_{\text{Al}}$ positions (Fig. 8d). Lath-shaped precipitates, mainly nucleated on dislocations in the STEM-DF image along $[001]_{\text{Al}}$ zone axis (Fig. 10d), are identified as S' precipitates, confirming results in Refs. [23,36]. Furthermore, apparent diffraction information of precipitates is absent in SAED patterns along $[011]_{\text{Al}}$ zone axis, signifying minor precipitation of the NZ.

In the Joints-AA, needle-shaped precipitates with high density are visible in the STEM-DF images along $[011]_{\text{Al}}$ zone axis (Fig. 8e). These are recognized as T_1 precipitates by the diffraction streaks along $[111]_{\text{Al}}$ direction in $[011]_{\text{Al}}$ zone axis (Fig. 7a). The platelet-shaped T_1 has four variants nucleating on the $(111)_{\text{Al}}$ habit planes, giving rise to easy detection of its two needle-shaped variants ($T_1^{2/4\#}$) of T_1 along $[011]_{\text{Al}}$ zone axis (Fig. 8a). While, two other variants ($T_1^{1/3\#}$) often exhibit an elliptical shape upon significant coarsening in thickness, as seen through spots at $1/3[022]_{\text{Al}}$ and $2/3[022]_{\text{Al}}$ positions in $[011]_{\text{Al}}$ SAED patterns (Fig. 8f). Therefore, the $T_1^{2/4\#}$ variants can be detected from the SAED patterns along $[001]_{\text{Al}}$ zone axis in Fig. 8h. Size distribution of the needle-like T_1 is summarized in Fig. 9a, indicating that the average radius ($r_{\text{Ave.}}$) and maximum radius ($r_{\text{Max.}}$) of these precipitates are 69.0 ± 15.9 nm and 110.6 nm, respectively. The spherical δ'/β' precipitates, visible in the STEM-DF images under the two diffraction directions, are identified by their spots at $1/2[022]_{\text{Al}}$ positions in the $[011]_{\text{Al}}$ SAED patterns, as well as the $1/2[002]_{\text{Al}}$ and $1/2[022]_{\text{Al}}$ positions in $[001]_{\text{Al}}$ SAED patterns (Fig. 8h). Another needle-like precipitates with 30–50 nm in length, seen in the STEM-DF images along $[011]_{\text{Al}}$ and $[001]_{\text{Al}}$ zone axis, are identified as θ' precipitates, suggesting the streaks along $[002]_{\text{Al}}$ direction in $[011]_{\text{Al}}$ SAED patterns, as well as $[002]_{\text{Al}}$ and $1/2[002]_{\text{Al}}$ direction in $[001]_{\text{Al}}$ SAED patterns. The finely dispersed rods precipitates seen in the $[001]_{\text{Al}}$ STEM-DF images are S' precipitates,

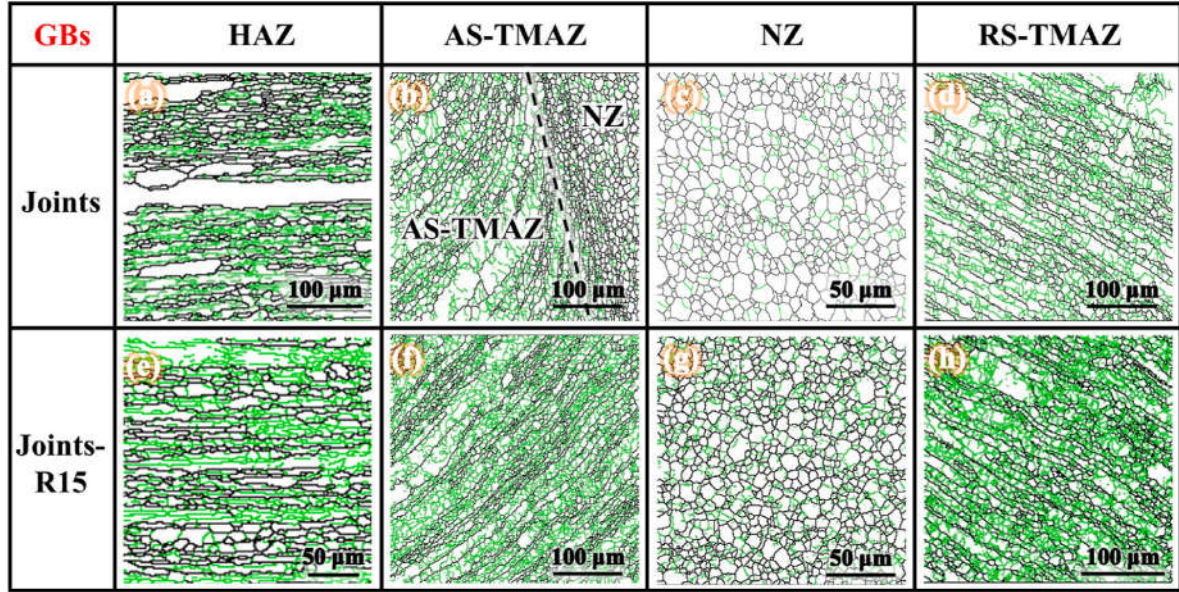


Fig. 5. GBs distribution of the HAZ, AS-TMAZ, NZ and RS-TMAZ for the (a–d) As-welded joints and (e–h) joints after rolling deformation.

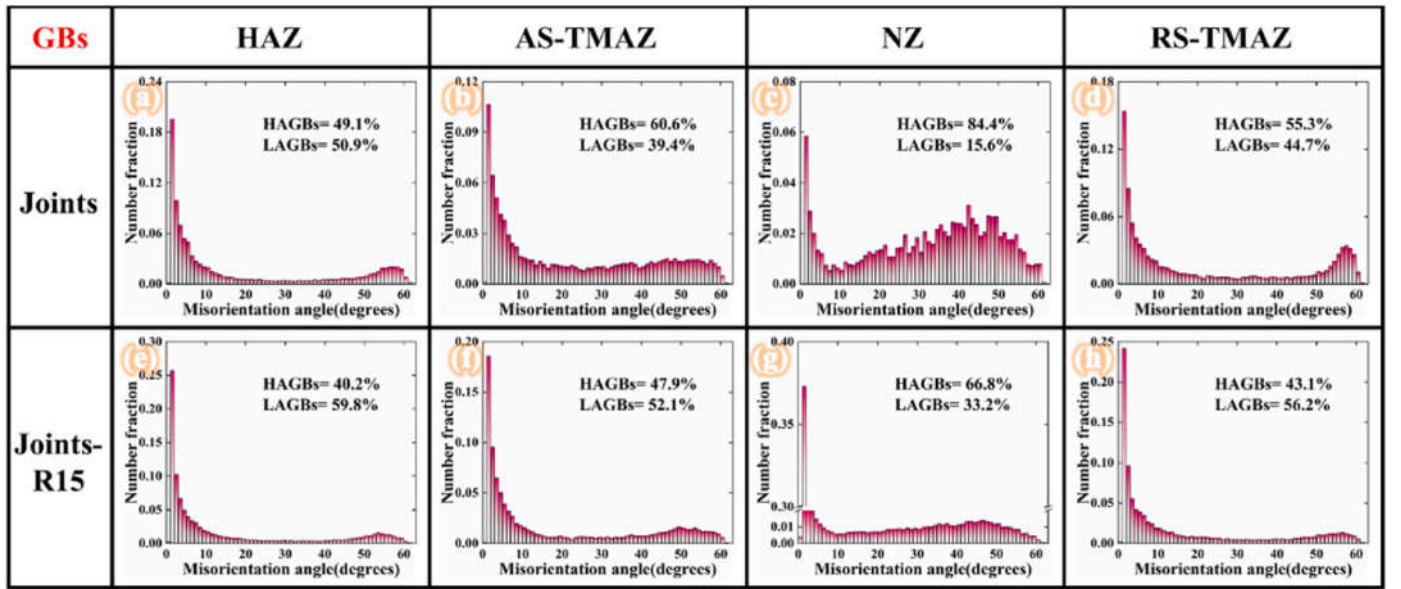


Fig. 6. GBs statistics of the HAZ, AS-TMAZ, NZ and RS-TMAZ for the (a–d) As-welded joints and (e–h) joints after rolling deformation.

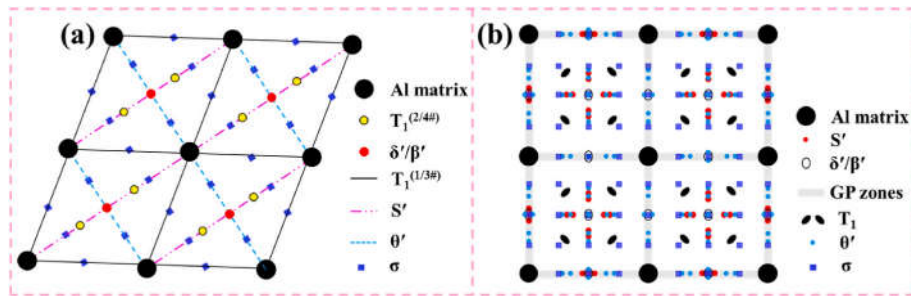


Fig. 7. Schematic SAED patterns of the main precipitates in 2195 Al-Li alloy along (a) $[011]_{Al}$ and (b) $[001]_{Al}$ zone axes.

recognizable by their streaks along $1/2[002]_{Al}$ direction in $[001]_{Al}$ SAED patterns.

In the Joints-R + AA (Fig. 8i–l), needle-like T_1 and θ' , spherical δ'/β'

are evident in the STEM-DF images and identifiable via the SAED patterns. The high density T_1 has 13.6 ± 4.2 nm and 27.2 nm in r_{Ave} and r_{Max} . (Fig. 9b), respectively, markedly lower than in the Joints-AA

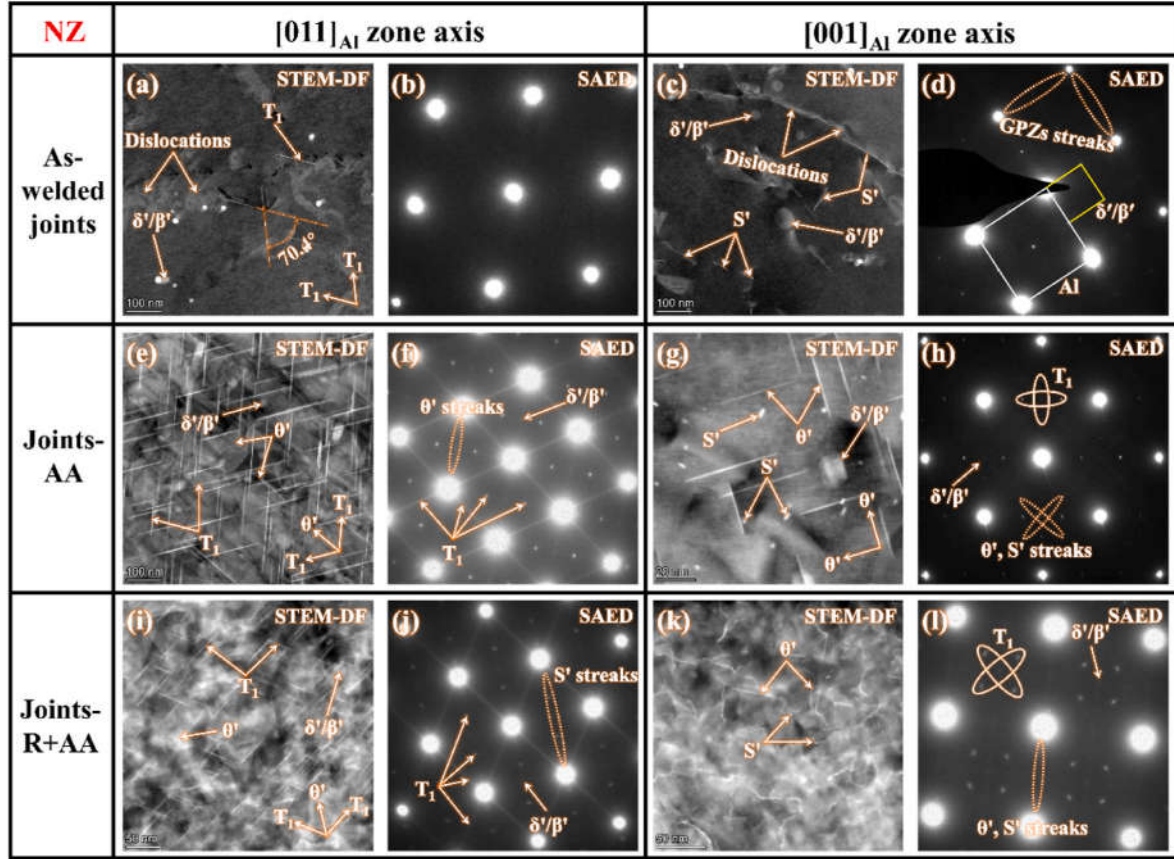


Fig. 8. STEM-DF and SAED images of the NZ in (a–d) As-welded joints, (e–h) Joints-AA and (i–l) Joints-R + AA along $[011]_{Al}$ and $[001]_{Al}$ zone axes.

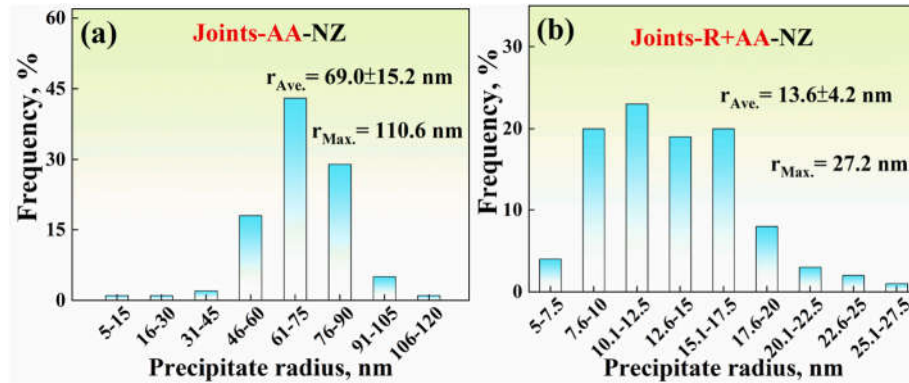


Fig. 9. Size distribution of T_1 in the NZ of (a) Joints-AA and (b) Joints-R + AA.

(Fig. 8a). The content of S' is obviously elevated, characterized by the faint streaks along the $[022]_{Al}$ direction in $[011]_{Al}$ SAED patterns and $1/2[002]_{Al}$ direction in $[001]_{Al}$ SAED patterns. Furthermore, two different morphologies of S' are observed, indicating that most of the precipitate is distorted with a long strip-shape, with a few showing fine, dispersed rod-shapes.

3.2.2.2. Precipitates in the TMAZ. Fig. 10 shows STEM-DF and SAED images of the TMAZ in the As-welded joints, Joints-AA and Joints-R + AA. Size distribution of T_1 in the TMAZ of Joints-AA and Joints-R + AA is shown in Fig. 12.

In the TMAZ of the As-welded joints, spherical δ'/β' precipitates are viewed in the STEM-DF images along $[011]_{Al}$ and $[001]_{Al}$ zone axes (Fig. 10a and c). While no obvious diffraction of this precipitate is

obtained in the SAED patterns (Fig. 10b and d), indicative of low-level precipitation in the TMAZ. Fig. 10a and c shows a newly developed cubic precipitate in $[011]_{Al}$ STEM-DF images yet clear in $[011]_{Al}$ STEM-DF images. This precipitate is identified as σ by the spots at $1/4[200]_{Al}$ and $1/4[220]_{Al}$ positions in $[011]_{Al}$ SAED patterns, as well as the spots at $1/5[002]_{Al}$ in $[001]_{Al}$ SAED patterns, as shown in Fig. 11. This found is close to the results reported in 2060 Al-Li alloy FSW joints [37]. Besides, dislocation tangle is common in this region.

In the TMAZ of Joints-AA (Fig. 10e–h) and Joints-R + AA (Fig. 10i–l), T_1 and θ' , δ'/β' , S' and σ are detected in the STEM-DF images, identified by spots in the SAED patterns along the two diffraction directions. T_1 , predominantly needle-shaped precipitate, appears larger in the Joints-AA compared to the Joints-R + AA (Fig. 12). The average size (r_{ave}) of T_1 is 65.2 ± 15.2 nm in Joints-AA, which is approximately 4.4 times

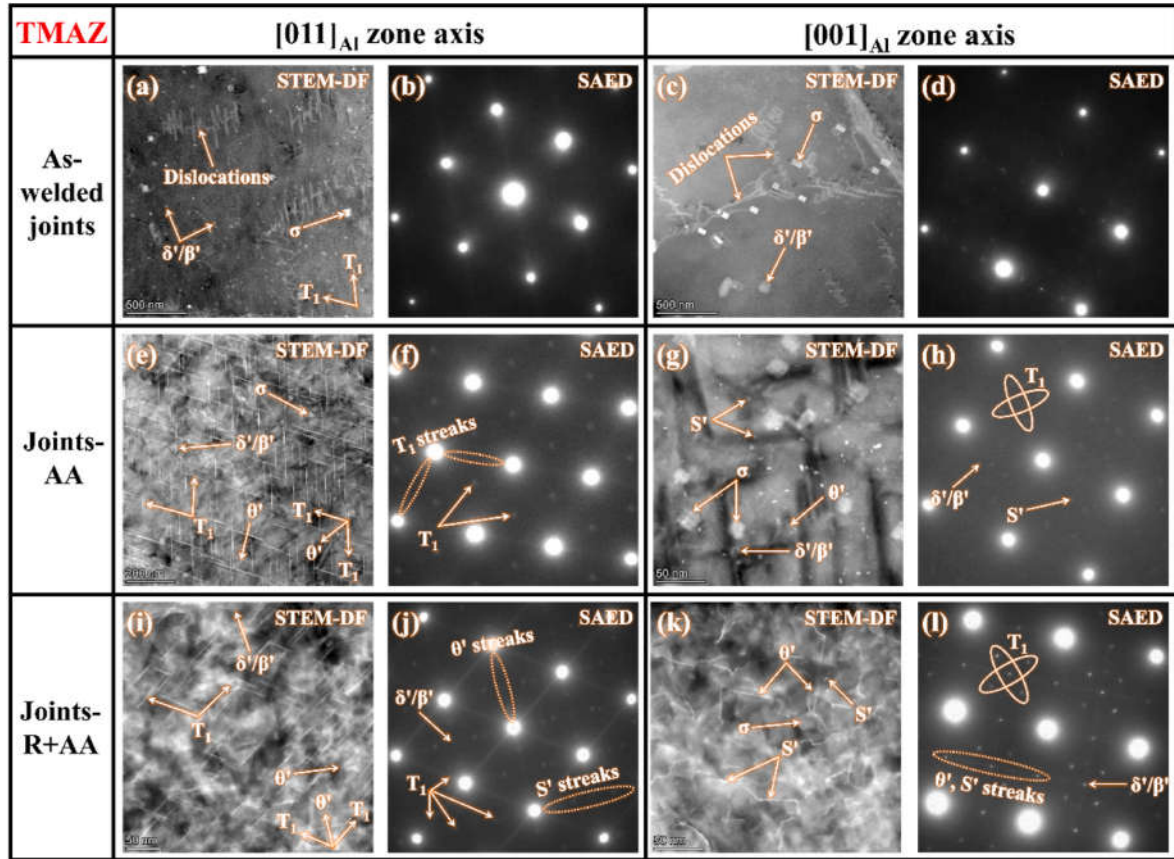


Fig. 10. STEM-DF and SAED images of the TMAZ in (a–d) As-welded joints, (e–h) Joints-AA and (i–l) Joints-R + AA along $[011]_{Al}$ and $[001]_{Al}$ zone axes.

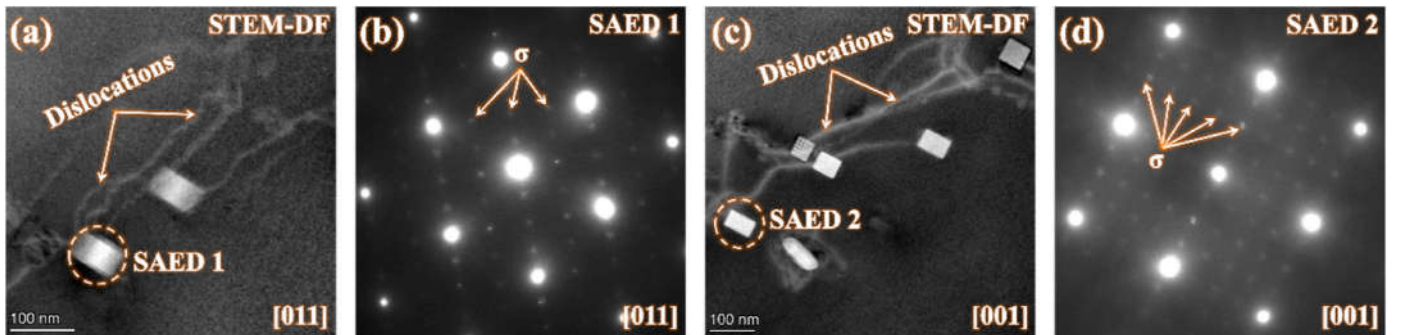


Fig. 11. TEM characterization of σ in the TMAZ of the As-welded joints by STEM-DF and SAED along (a) $[011]_{Al}$ zone axis and (b) $[001]_{Al}$ zone axis.

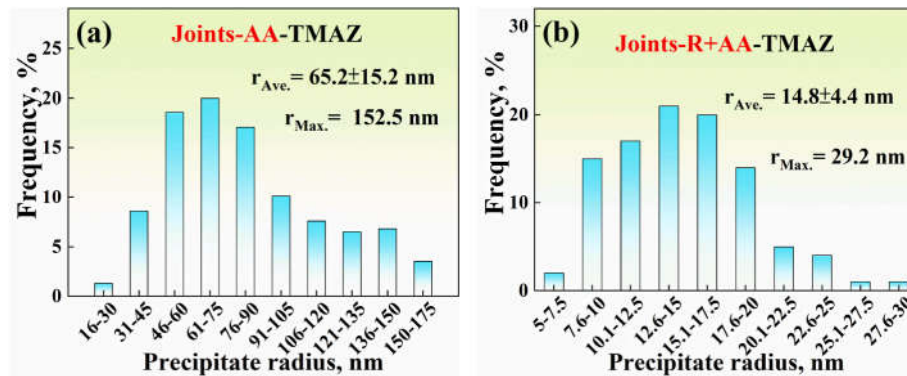


Fig. 12. Size distribution of T_1 in the TMAZ of (a) Joints-AA and (b) Joints-R + AA.

larger than in the Joints-R + AA (14.8 ± 4.4 nm). The r_{Max} of T_1 is 5.2 times higher in Joints-AA (152.5 nm) compared to that in Joints-R + AA (29.2 nm). S' appears as finely dispersed rods in Joints-AA (Fig. 10g) but mainly takes a long strip-shape in Joints-R + AA (Fig. 10k).

3.2.2.3. Precipitates in the LHZ. In this study, negligible LHZ can be observed in the As-welded joints, while this feature obviously appears after aging treatment. These correlations are significant with the evolution of precipitates in the LHZ. Hence, TEM characterization of precipitates was performed in the LHZ as shown in Fig. 13. The size distribution of T_1 in these regions is illustrated in Fig. 15.

In the LHZ of the As-welded joints, the needle-like precipitates in $[011]_{\text{Al}}$ STEM-DF images signify T_1 (Fig. 13a), which are recognizable by their diffraction streaks along $[111]_{\text{Al}}$ direction in $[011]_{\text{Al}}$ SAED patterns (Fig. 14c). In addition, some elliptical-shape zones exhibiting light contrast are often observed in this region. These precipitates, proven by spots at $1/3[220]_{\text{Al}}$ and $2/3[220]_{\text{Al}}$ positions in $[011]_{\text{Al}}$ SAED patterns (Fig. 14d), are another two variants of T_1 . δ'/β' , σ and θ' precipitates are also found in the LHZ. Precipitate free zone (PFZ) adjacent to grain boundary phases (GBPs) is viewed with a width exceeding 400 nm.

In the LHZ of Joints-AA (Fig. 13e–h) and Joints-R + AA (Fig. 13i–l), T_1 , θ' , δ'/β' , S' , σ , GBPs and PFZ are observed in the STEM-DF images. The main precipitates can be determined according to the SAED patterns along the two diffraction directions. The morphology of T_1 remains largely consistent, exhibiting a needle shape. However, their size distribution varied significantly in both joints. Two different sizes of the needle-shaped T_1 precipitates are generated in the LHZ of Joint-R + AA. Fine, needle-shaped T_1 with a radius between 5 nm and 30 nm are found in this region, while the coarse ones have a size of 121–270 nm (Fig. 15c). The size of T_1 within the LHZ of Joint-AA lies between 20 nm and 200 nm, matching closely the precipitate (36–195 nm) in the As-

welded joints displayed in Fig. 15a and b. Notably, the average size ($r_{\text{Ave.}}$) of T_1 in the LHZ shows As-welded joints > Joints-AA > Joints-R + AA, while the maximum size (r_{Max}) decreases in another order, As-welded joints < Joints-AA < Joints-R + AA. GBPs commonly display continuous distribution within the LHZ of Joints-AA, contrasting with its scarce detection in Joints-R + AA. The PFZ width varies around 270 nm in the LHZ of Joints-AA and 195 nm in the LHZ of Joints-R + AA, which both notably narrower than the observed PFZ width in the As-welded joints (Fig. 13a).

3.2.2.4. Precipitates of the HAZ. Fig. 16 shows STEM-DF and SAED images of the HAZ in the As-welded joints, Joints-AA and Joints-R + AA. Fig. 17 presents the size distribution of T_1 in the HAZ of the three joints.

In the As-welded joints, a few small T_1 precipitates with needle shape is formed on sub-grain boundaries and dislocations, visually identified in the $[011]_{\text{Al}}$ STEM-DF images (Fig. 16a and b). Spherical δ'/β' precipitates are found in both $[011]_{\text{Al}}$ and $[001]_{\text{Al}}$ STEM-DF images (Fig. 16a and c). GPZs are detected by the diffraction streaks in the $[001]_{\text{Al}}$ SAED patterns (Fig. 16d).

The HAZ of Joints-AA (Fig. 16e–h) and Joints-R + AA (Fig. 16i–l) contain T_1 , θ' , δ'/β' , S' , σ , identifiable through their morphology and the SAED patterns along $[011]_{\text{Al}}$ and $[001]_{\text{Al}}$ zone axes. Two sizes of T_1 exist in the Joints-R + AA, with the fine precipitates develop radius between 5 nm and 30 nm, while the coarse ones range from 45 nm to 195 nm (Fig. 17c). The average radius ($r_{\text{Ave.}}$) of T_1 in the Joints-AA is 50.7 ± 17.5 nm, over three times higher than in the Joints-R + AA. Conversely, the maximum radius (r_{Max}) of T_1 in the Joints-R + AA (193.4 nm) is approximately twice of that in Joints-AA (95.1 nm). Grain boundary phases (GBPs) are generated in the HAZ of Joints-AA, but seldom observed in the HAZ of Joints-R + AA.

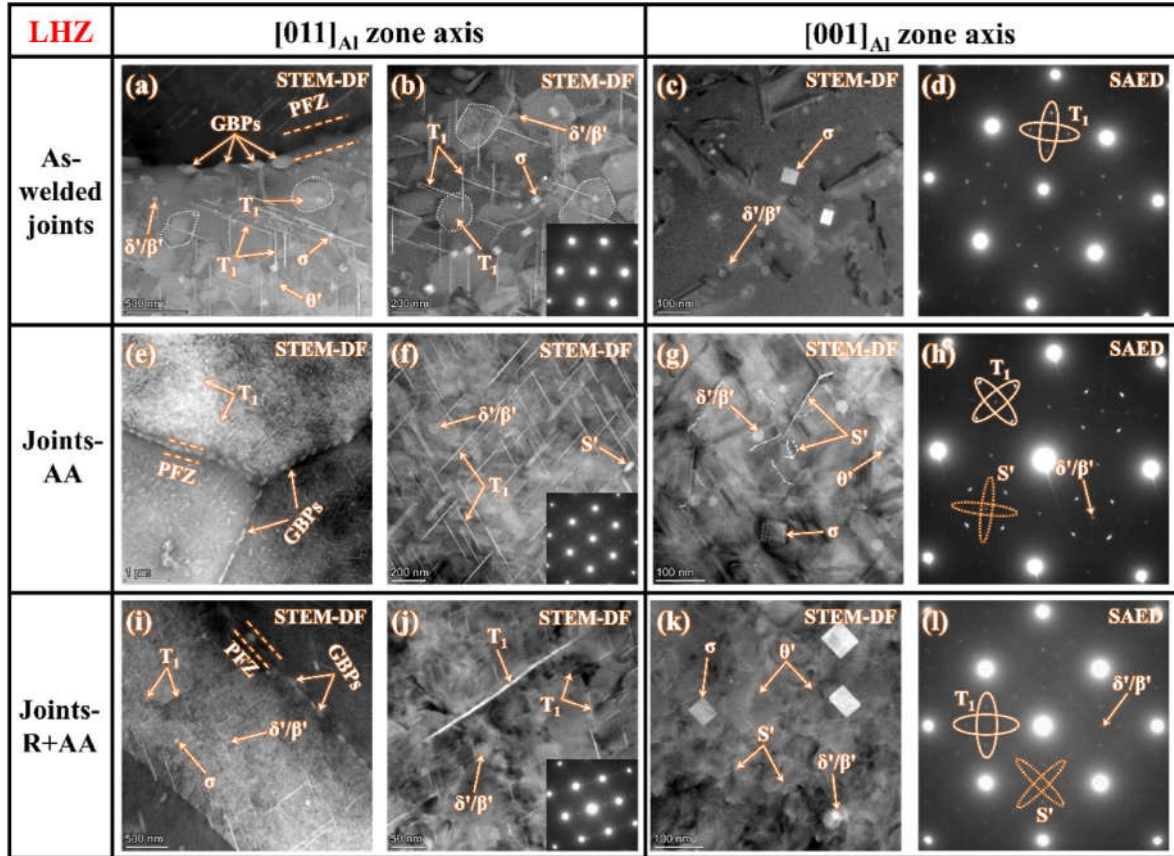


Fig. 13. STEM-DF and SAED images of the LHZ in the (a–d) As-welded joints, (e–h) Joints-AA and (i–l) Joints-R + AA along $[011]_{\text{Al}}$ and $[001]_{\text{Al}}$ zone axes.

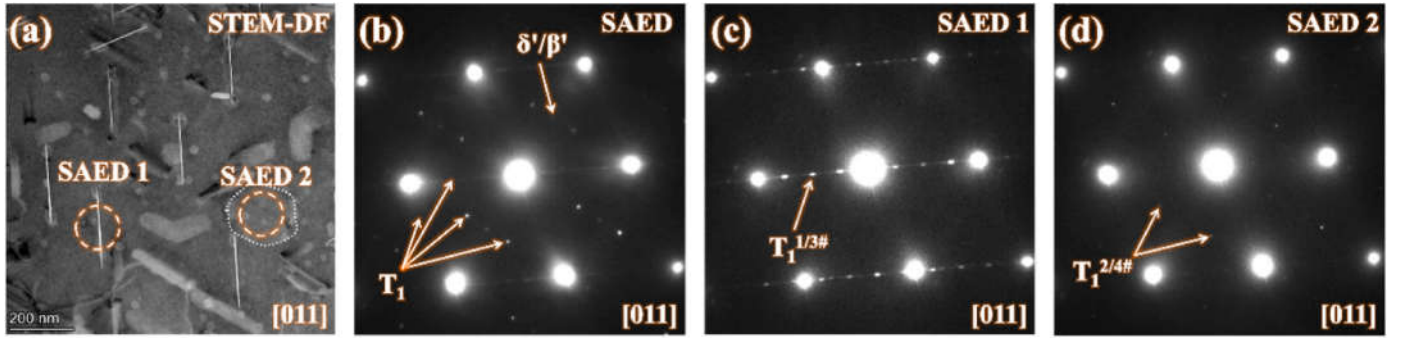


Fig. 14. TEM characterization of T_1 in the LHZ of the As-welded joints by (a, b) STEM-DF and corresponding SAED along $[011]_{Al}$ zone axis, (c) SAED1 for the needle-like T_1 and (d) SAED2 for the elliptical-shape T_1 .

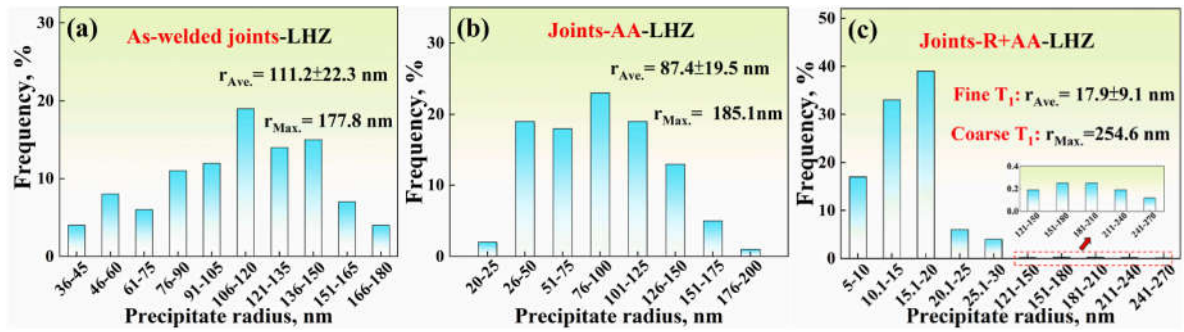


Fig. 15. Size distribution of T_1 in the LHZ of (a) As-welded joints, (b) Joints-AA and (c) Joints-R + AA.

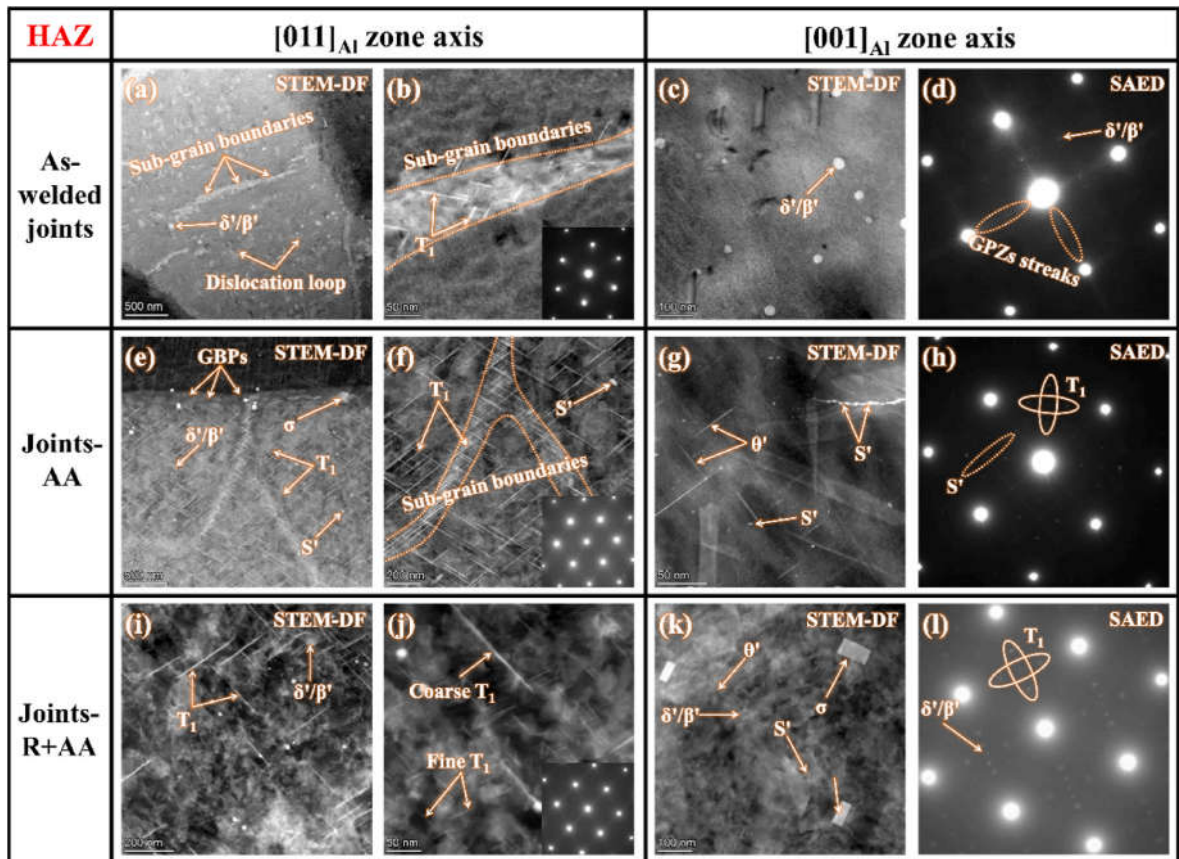


Fig. 16. STEM-DF and SAED images of the HAZ in (a–d) As-welded joints, (e–h) Joints-AA and (i–l) Joints-R + AA along $[011]_{Al}$ and $[001]_{Al}$ zone axes.

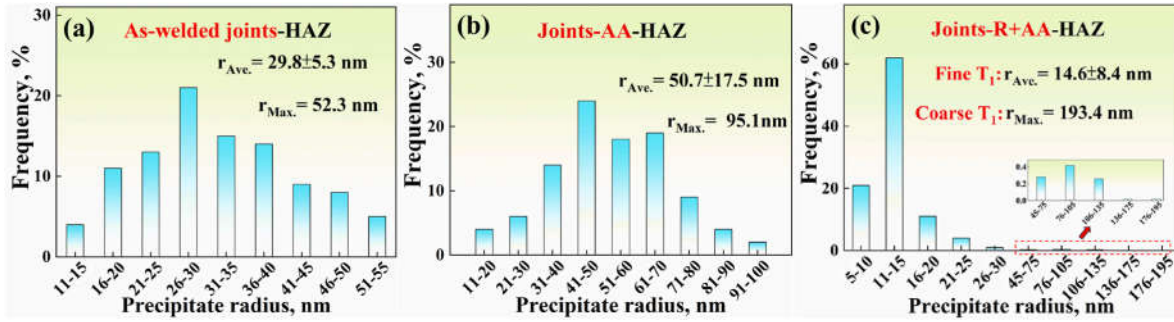


Fig. 17. Size distribution of T_1 in the HAZ of (a) As-welded joints, (b) Joints-AA and (c) Joints-R + AA.

3.3. Tensile properties

Fig. 18 shows engineering stress-strain curves and tensile properties of the As-welded joints, Joints-AA and Joints-R + AA. Table 3 provides tensile test results the three joints. Analysis of their tensile properties yields several insights: Firstly, the As-welded joints possess the lowest ultimate tensile strength (UTS) and the maximum elongation, indicating that the joint strength increases but the elongation decreases after PWHT. Secondly, both UTS and elongation of Joints-R + AA surpass those of Joints-AA, implying that rolling deformation can improve both strength and plasticity of artificially aged 2195-T4 Al-Li alloy FSW joints. Thirdly, all three joints are failing in the LHZ in a tensile test, potentially indicating a similar fracture mechanism. Fig. 19 displays the fracture morphologies of these joints for further clarification of the fracture behavior.

Fracture surfaces of the three joints exhibit pronounced intergranular cracks aligning with coarse elongated grains, initiating cleavage facets, steps, and fine dimples. Additionally, micro-voids with cracked particles at the bottom are frequently produced adjacent to intergranular cracks within these joints. Notably, dimples generate in As-welded joints, appear scarcely in Joint-AA, and barely detectable in Joints-R + AA, signifying toughness fracture as the primary mode of failure in the As-welded joints compared to brittle fracture in Joints-AA and Joints-R + AA.

4. Discussion

4.1. Microstructure evolution

4.1.1. Grains

In this study, the BM, an Al-Li alloy in natural aged condition, originated from hot-rolled plates via solution and natural aging. The grains of the hot-rolled plates exhibit a typical layered structure with numerous LAGBs. Despite the high temperature during the solid solution treatment promote the occurrence of static recrystallization, a short-duration solution treatment hardly makes full recrystallization. Hence,

Table 3

Tensile test data of three joints.

| Joints | UTS (MPa) | Elongation (%) | Fracture location |
|------------------|---------------|----------------|-------------------|
| As-welded joints | 440.0 ± 6 | 13.5 ± 0.5 | LHZ |
| Joints-AA | 506.5 ± 9 | 3.4 ± 0.6 | |
| Joints-R + AA | 530.5 ± 7 | 3.9 ± 0.4 | |

the BM comprises elongated grains, high percentages of LAGBs and substructures (Figs. A-1).

During the FSW, the HAZ is mostly influenced by the welding thermal cycle and experiences recovery, demonstrating identical microstructure properties with the BM [38]. Within the TMAZ, materials are subjected to extrusion from shoulders and mixing needles with grains curved along the material flow of the NZ [39]. Simultaneously, dynamic recrystallization occurs under the high temperature of the NZ. However, insufficient degree of material deformation and peak temperature do not permit complete recrystallization in the TMAZ. The internal grain misorientation diminishes during recrystallization, transforming LAGBs to HAGBs. Consequently, the content of LAGBs in the TMAZ is lower than in the HAZ. Plastic deformation makes grains rotation leading to grain orientation changing, and the recrystallization behavior further distorts the orientation, hence the grain orientation features of the TMAZ greatly differ from those of the HAZ, becoming more random. It has been demonstrated that materials on the advancing side of the NZ experience a more extreme deformation and higher temperature [40], enhancing the degree of recrystallization in AS-TMAZ, reducing the content of LAGBs, while the content of recrystallization increasing significantly. Due to the severe thermomechanical action, grains in the NZ conclude full recrystallization through dynamic recrystallization, generating fine recrystallized grains, which significantly reduce the content of LAGBs.

Rolling deformation amplifies strain and average misorientation within the grains, leading to an increase of LAGBs. As the rolling deformation is relatively low, the variations in grain morphology and orientation are limited.

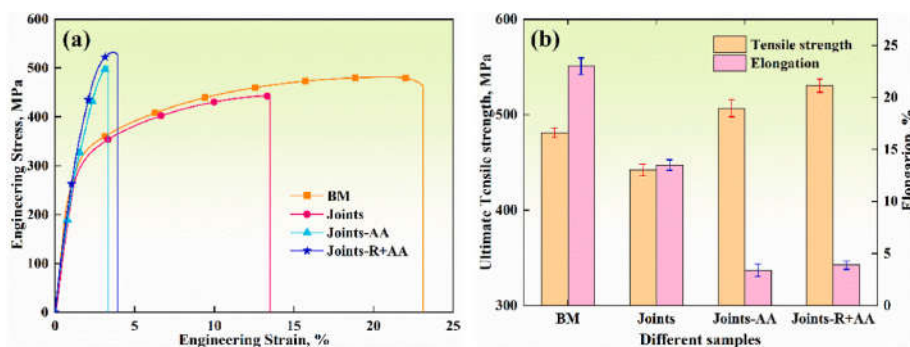


Fig. 18. Tensile test results of (a) Engineering stress-strain curves and (b) the ultimate tensile strength and elongation of the BM and three joints.

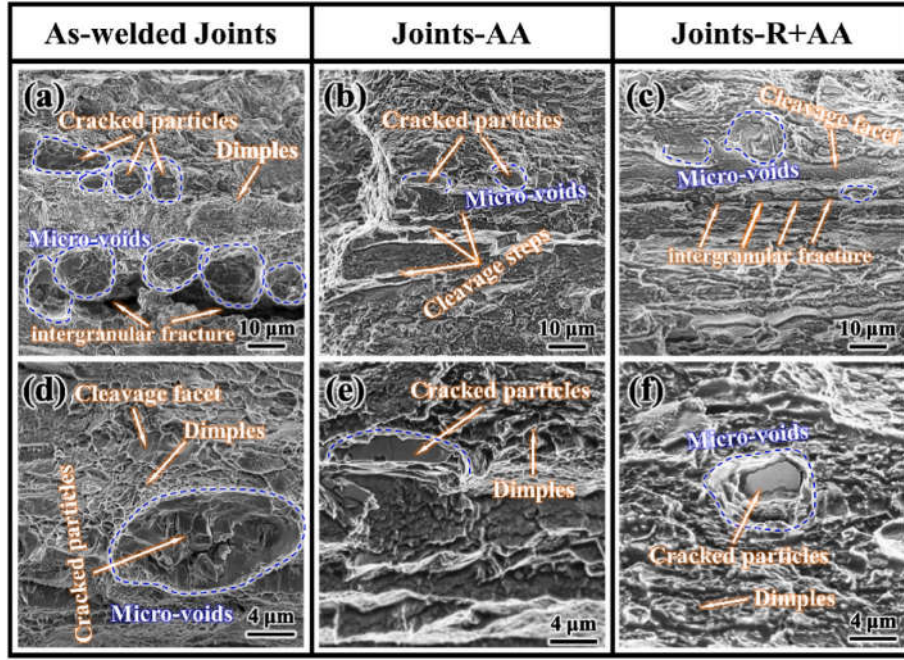


Fig. 19. Fracture morphologies of (a, d) As-welded joints, (b, e) Joints-AA, (c, f) Joints-R + AA.

4.1.2. Precipitates

4.1.2.1. Precipitates in base material. In the quenched 2195 alloy, micro-alloy elements primarily reside within the matrix, leading to a dense population of clusters GPZs forming. Both δ' and β' have low misfit and interface energy with Al matrix, making them primary precipitates at 90–120 °C, easily nucleating during natural aging [41]. Thus, GPZs, δ' and β' are found in the BM (Fig. A-1c and Fig. A-1d), under T4 (natural aging) temper conditions.

4.1.2.2. Precipitates evolution in different joints. During FSW, the NZ suffers the highest welding temperature, commonly 450–550 °C in Al alloys [42]. Peak temperature in the TMAZ is lower than in the NZ, and is usually obtained above 400 °C [43]. The HAZ is subjected to the lowest welding temperature, and the maximum temperature invariably exceeds 350 °C [44,45]. The thermal history of FSW joints, impacted by the elevated temperature, can be segmented into three distinctive stages. These stages not only dissolve precipitates but encourage new precipitate nucleation and growth. The initial stage occurs during the welding, in which the high welding temperature causes δ'/β' dissolving and GPZs decomposing. The second stage takes place post-weld, at a residual temperature over 120 °C, offering an artificial aging treatment and resulting in precipitate formation and coarsening. Factors like the varying residual temperature facilitate the nucleation of T_1 and S' in the NZ, σ formation in the TMAZ, and T_1 generation in the HAZ. These precipitates have a minute size and number due to the brief duration of thermal effect. The final stage occurs below 120 °C, where δ'/β' and GPZs reform.

Upon sufficient artificial aging, T_1 densely form the dominant strengthening phase in Joints-AA. T_1 is the major strengthening precipitate in 2195 Al-Li alloy, whose preferential sites for nucleation include dislocations, LAGB interface, stacking faults and vacancy clusters. With adequate aging, there is minimal disparity in stacking fault and vacancy clustering across joint regions. The LAGBs in different regions have been identified by EBSD data, revealing an order of contents HAZ > TMAZ > NZ, represented in Fig. 5. Dislocation density can be quantified using kernel average misorientation (KAM) method, calculated based on local misorientation from EBSD data [46,47]. The local crystal orientation within various regions is determined through the

geometrically necessary dislocation (GND) evolution. Notably, misorientation exceeding 2° is discounted in this analysis. The local misorientation at a point is determined through its 24 neighboring points [46]:

$$\Delta\theta_i = \frac{1}{n} \sum_{j=1}^n |\theta_j - \theta_i|$$

Where θ_i represents the local misorientation at the point 'i' and θ_j means the misorientation at its neighboring points 'j'; $\Delta\theta_i$ represents local misorientation. The GND density (ρ^{GND}) can be determined by a simple method according to the strain gradient theory as follows [48,49]:

$$\rho^{\text{GND}} = \frac{2\Delta\theta_i}{\mu b} = B\Delta\theta_i$$

Where μ is the step size selected for the EBSD experiment; b the Burgers vector. $B = 2b \cdot 10^{16} \text{ m}^{-2}$, is a constant in this study. As illustrated in Fig. 20, KAM and GND density varies across different zones within As-welded joints. It is obvious that the average GND density ($\rho_{\text{av}}^{\text{GND}}$) showing an overall trend of HAZ > AS-TMAZ > NZ. The increased presence of LAGBs and dislocations results in more nucleation sites and accelerated precipitation kinetics. Therefore, the artificially aged joints reveal the average size of T_1 to be HAZ < AS-TMAZ < NZ.

Cold work prior to artificial aging has been demonstrated to increase the amount of intra-granular precipitation of T_1 , which is attributed to the increase in dislocation density and therefore potential nucleation sites in the formation of high strain fields. Fig. 21 shows the KAM and GND density across different regions of the rolling deformation joints. The dislocation density of these regions is increased after rolling deformation, indicating more nucleation sites for T_1 generation. Thus, significantly smaller in size and bigger in density of T_1 is developed in the Joints-R + AA. In addition, average size of T_1 is very close in the HAZ, AS-TMAZ and NZ of the Joints-R + AA, likely due to minimal differences in dislocation density post-rolling deformation. In the HAZ, the increased maximum size of T_1 dimension results from further coarsening of initial T_1 during PWHT. The coarsening process generally presents greater resistance than precipitation process, making T_1 coarsening more challenging [50,51]. Hence, the unremarkable increase of the maximum size occurs in the Joints-AA. However, pre-rolling deformation leaves a large quantity of dislocations in the LHZ, which

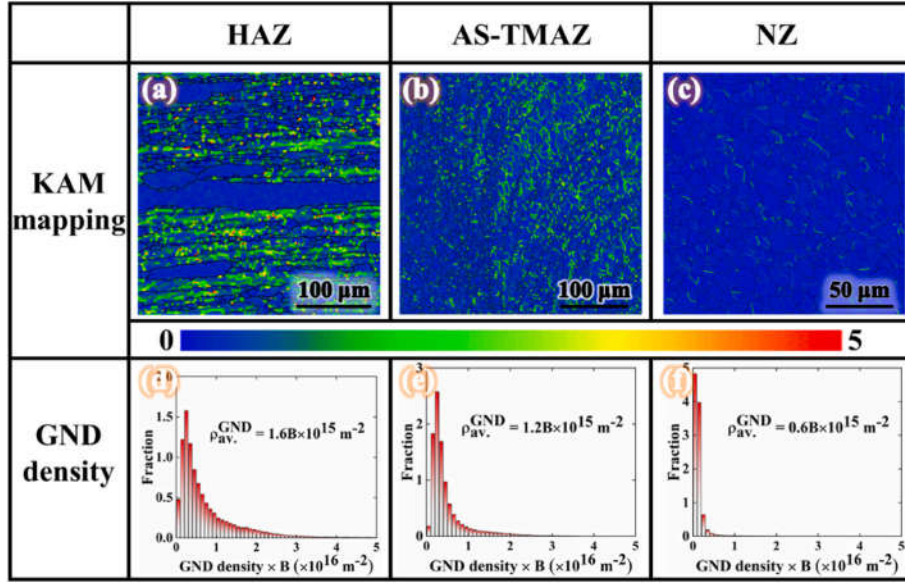


Fig. 20. The EBSD analysis results of the HAZ, AS-TMAZ and NZ about (a–c) KAM mapping and (d–f) GND density distribution statistics.

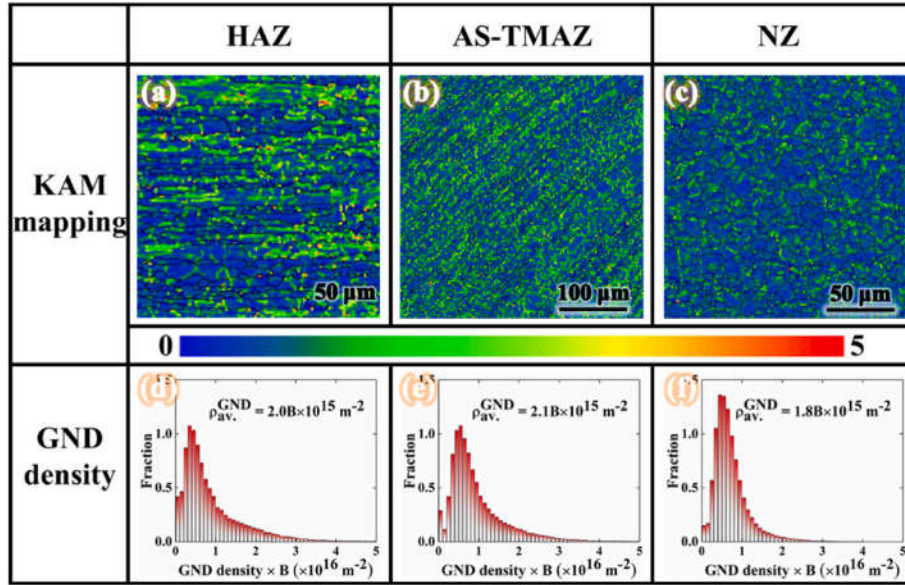


Fig. 21. The EBSD analysis results of the 15 % rolling joints involving in (a–c) KAM mapping and (d–f) GND density distribution statistics to the HAZ, AS-TMAZ and NZ.

interact intensely with pre-existing T_1 and accelerate the segregation of solute atoms during heat treatment along the interface between T_1 phase and Al matrix, culminating in an abnormally coarse T_1 in the LHZ of the Joints-R + AA.

4.2. The development of the LHZ

Generally, the LHZ is a typical feature in artificial aging status (commonly T6 or T8) Al alloy FSW joints [42]. In this study, the LHZ is inapparent in As-welded joints, but obviously developed after artificial aging. The LHZ is positioned within the HAZ and close to the TMAZ. The thermal-mechanical history of the LHZ approximates that of the HAZ. Consequently, the evolution rule of precipitate in the LHZ mirrors that in the HAZ. A greater precipitation degree develops in the LHZ due to higher peak temperature compared to the HAZ, leading to a larger size and amount of T_1 formation, as well as more distinct GBPs and PFZ.

Artificial aging treatment can promote an abundance of T_1 precipitation, resulting in considerable growth in the number of T_1 in the Joints-AA. PWHT operates at lower temperatures than the peak welding temperature of the LHZ, reducing the precipitation size of T_1 and consequently decreasing the average size of T_1 in the LHZ of the Joints-AA. Pre-deformation can increase the nucleation sites of T_1 , leading to dense and small T_1 in Joints-R + AA. The significant increase in the maximum size of T_1 in the LHZ is due to further coarsening during the PWHT for the previously formed T_1 , as observed in the HAZ of the joints.

The tiny T_1 can efficaciously impede dislocation motion, enhancing the strength and hardness of 2195 Al-Li alloy. However, the strengthening impact of coarse precipitates is marginal. Moreover, the formation of GBPs and PFZ hinder the enhancement of LHZ hardness. The elevated welding temperature promotes the formation of coarse T_1 and GBPs in the LHZ, which fails to yield precipitation strengthening effects and reduces the concentration of solute atoms in the matrix, reducing the

solid solution strengthening effects. Consequently, the hardness of this region is inferior to that of other areas in the joint. Due to the brief high-temperature duration of the welding process, the extent of solute precipitation is overall small, and the hardness of LHZ does not significantly diminish. Artificial aging enhances T_1 precipitation, leading to a significant increase in the T_1 density of Joints-AA and Joints-R + AA, and consequently, the hardness increases significantly. However, the hardness on both sides of the transition area between the TMAZ-HAZ increases modestly, signifying insufficient precipitation of T_1 in these regions. Fig. 22 illustrates the number density of T_1 in the different regions of the three joints. It is evident that the T_1 number density in As-welded joints is exceedingly small, significantly less than that in the two other joints, indicating a minimal contribution of T_1 to strength. After artificial aging, the density of T_1 increases substantially but not uniformly across different zones. The density of T_1 in LHZ is comparatively lower, showing a trend that is consistent among Joints-AA and Joints-R + AA. Moreover, in these two joints, the density of T_1 and joint hardness demonstrate a close correlation.

Malard et al. [52] established that the precipitation dynamics of the FSW joints during PWHT primarily depend on solute content and dislocation density available for precipitation. In the As-welded joints, the solute concentration in the LHZ is less than other zones, leading to reduced precipitation of T_1 and a smaller increase in its density after artificial ageing. Hence, the hardness enhancement is minimal, causing an increased disparity with neighboring zones, resulting in significant LHZ. Pre-deformation elevates dislocation density across all zones of the joint, reduces the nucleation barrier of precipitates [53], enhances precipitation dynamics in LHZ, and promotes abundant precipitation of T_1 during post-aging. Large amounts of fine T_1 significantly enhance the hardness of the LHZ. For Joints-AA, a solitary artificial ageing treatment brings the hardness of BM and NZ regions closer to the peak hardness of this alloy. Pre-straining does not notably enhance the hardness in these zones after artificial aging, but can further increase the hardness of the LHZ. As a result, less hardness enhancement is noted in the BM and NZ of the Joints-R + AA, while the hardness near LHZ increases more, minimizing the fluctuation range of joint hardness distribution.

4.3. Tensile properties of the different joints

In this research, post-weld artificial aging treatment promotes T_1 precipitation, dramatically enhancing tensile strength of Al-Li alloy FSW joints. Coupled with pre-rolling deformation, it effectively controls T_1

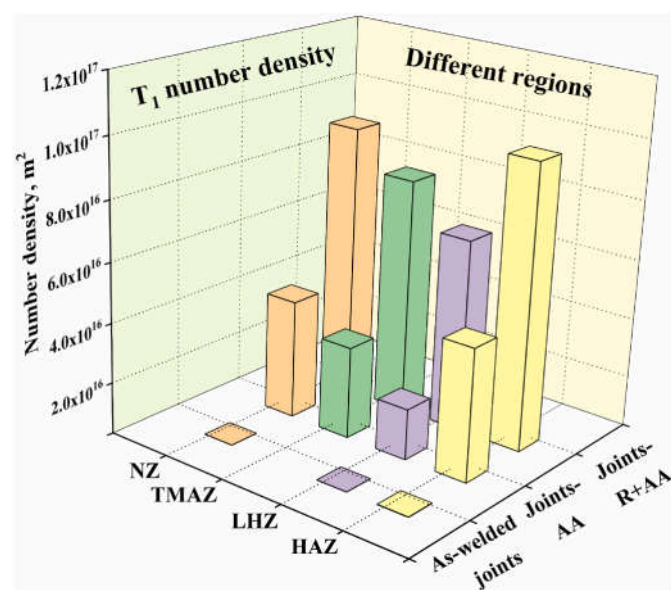


Fig. 22. Number density statistics of T_1 in typical regions of different joints.

precipitation volume and size during the artificial aging, leading to dense and fine T_1 in the joint, reinforcing the softening regions (the LHZ) and further elevating joint strength. The strength of Joints-R + AA is approximately 530.5 MPa, reaching 96.4 % of 2195-T6 Al-Li alloy and 88.3 % of 2195-T8 Al-Li alloy. This implies that a high-strength Al-Li alloy FSW joint can be attained via post-weld heat treatment involving pre-deformation and artificial aging. Mostly, strength and ductility are conflicting attributes, i.e., higher strength results in reduced ductility, vice versa. Herein, the enhancement of joint strength resulted from post-weld artificial aging is at the expense of joint ductility. Therefore, the elongation levels of Joints-AA and Joints-R + AA have decreased significantly. Significantly, compared with Joints-AA, the pre-rolling method not only enhances the joint strength but also improves its elongation, defying conventional strength-ductility correlations.

The hardness results have verified that pre-deformation and artificial aging can further enhance micro-hardness of the LHZ, reducing joint hardness distribution fluctuations. This conclusion is further analyzed through hardness mapping analysis, as shown in Fig. 23. It is easy to find that the overall hardness value in the As-welded joints is low, with a disparity in minimum and maximum hardness of approximately 20 HV. Post artificial aging treatment escalated the hardness for Joints-AA, but amplifies the disparity in maximum and minimum hardness to approximately 50 HV. As a result, the softening zones expand and the uniformity of the joint diminishes. Conversely, pre-rolling deformation greatly diminishes the disparity (30 HV) in maximum and minimum hardness in the Joints-R + AA compared to the Joints-AA. Thus, hardness uniformity of the joint after pre-deformation and artificial aging increases, resulting in a superior uniform deformation ability and joint ductility. The pre-deformation method efficiently addresses the issue of joint softening after artificial aging and enhances the uniform deformation ability of the joint, leading to superior fracture elongation in Joints-R + AA compared to Joints-AA.

Fig. 24 shows the comparison of tensile performance of various Al-Li alloy FSW joints, with light purple zone denoting untreated FSW joints and yellow zone representing heat-treated joints. It is discernible that most researchers employ artificially aged (T6 and T8) Al-Li alloys in FSW experiments, seldom utilizing naturally aged (T4) ones [31,33–35]. Therefore, the present study broadens the understanding of the FSW process involving Al-Li alloys. Mechanical properties of similar materials in various literature vary considerably, primarily due to the difference of welding process parameters, parent material performance and FSW equipment [3,13,54]. Generally, high Cu/Li ratio 2195 and 2060 Al alloys exhibit elevated FSW joint strength, with the maximum strength reaching 490 MPa from a 2060-T8 Al-Li alloy [55]. There are substantial variations in elongation among artificially aged Al-Li alloy FSW joints, but those of naturally aged (T4) Al-Li alloy achieve superior values and stable results. In this study, the As-welded joints have excellent strength of 440 MPa (91.7 % joint coefficient) and remarkable elongation of 13.5 %. Notably, this elongation is an exceptionally high value in published literature. This indicates that using naturally aged 2195 Al-Li alloy for FSW can result in the joint with satisfactory tensile performance. In actual production, the manufacturing process of naturally aged Al-Li alloy is simpler and more economical compared to artificially aged Al-Li alloy. Thus, it could be financially advantageous in specific conditions to utilize the naturally aged alternative over the artificially aged alloy for friction stir welding.

Post-weld heat treatment (PWHT) is one of the important measures to improve the mechanical properties of FSW joints. Relevant research is common in 6xxx and 7xxx Al alloys, but there are few reports on Al-Li alloys [30,32,68]. Currently, only a few related articles have been found, as shown in the yellow area in the upper left corner of Fig. 24. These papers suggest that the PWHT for Al-Li alloy FSW joints enhances joint strength by controlling the precipitation of T_1 . Zhang et al. [11] achieves a marked rise in joint strength from 367.3 MPa to 480.3 MPa (about 30.8 %) via solid solution and artificial aging (SAA) processing on 2195-T8 Al-Li alloy FSW joints, but the strength post-heat treatment is

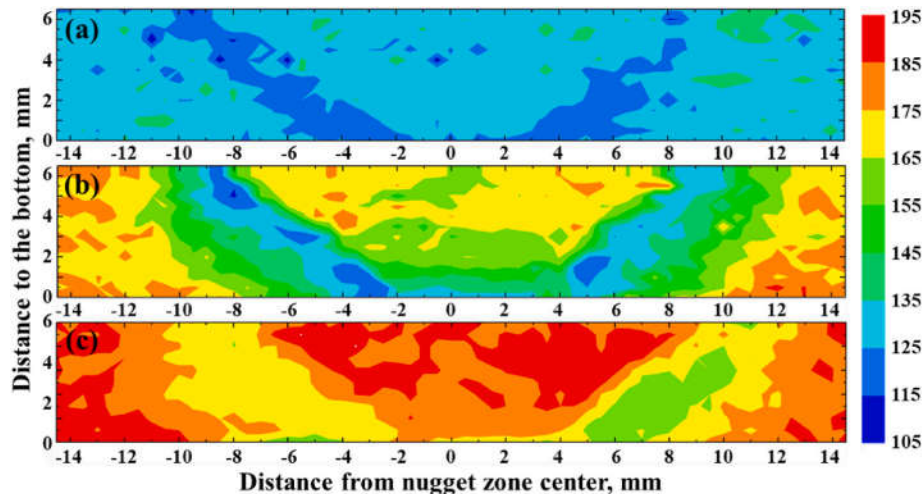


Fig. 23. Hardness mapping of (a) As-welded joints, (b) Joints-AA, (c) Joints-R + AA.

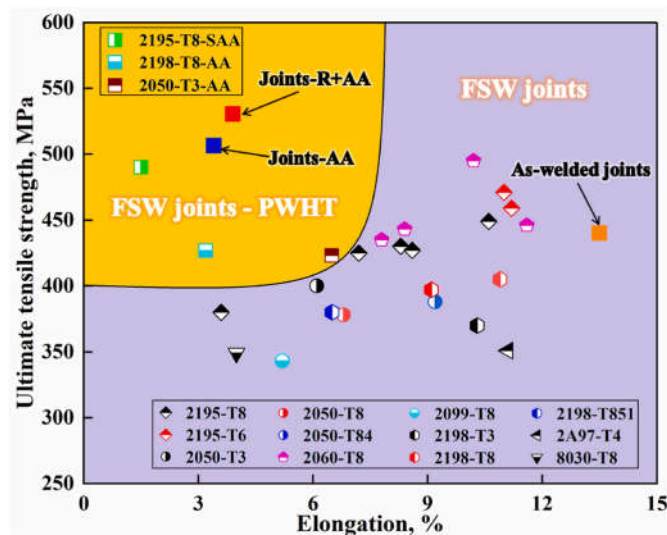


Fig. 24. Comparison of elongation and ultimate tensile strength between the present results and other available data of Al-Li FSW joints (including As-welded joints and PWHT joints) [10,11,21–24,45,55–67].

still relatively low, only at 85 % of the parent material strength. More critically, abnormal grain growth (AGG) occurs in the NZ during solid solution treatment, resulting in a significant reduction in fracture elongation of the treated joints and damages comprehensive performance of the joint. Indeed, due to stability issues in the grain of the NZ, post-weld solid solution processing often causes this AGG, deteriorating the plasticity of the joint post-heat treatment [29,32,69]. Some scholars choose to directly perform artificial aging treatment on FSW joints, effectively avoiding the AGG problem and improving the joint strength to a certain extent [33,64]. However, the strength improvement is relatively limited and has not yet exceeded 500 MPa, failing to obtain high-strength Al-Li alloy FSW joints. The primary reason behind this result is the precipitation state and composition limitation of the BM, causing the T_1 not to precipitate significantly during artificial aging treatment. In this research, due to the use of 2195 Al-Li alloy in a natural aging state and possessing a high Cu/Li ratio, post-weld artificial aging treatment can promote the formation of high-density of T_1 , significantly improving the joint strength. Furthermore, integrating pre-deformation technology can efficiently control the density and size of T_1 in the LHZ, allowing the achievement of a strength of 530.5 MPa and a high-strength

joint.

5. Conclusions

In this study, the effect of different post-treatments on microstructure and mechanical properties of friction stir welded 2195-T4 Al-Li alloy joints were investigated. The main conclusions are as follows:

- (1) During FSW, the overall precipitation level of the As-welded joint remains minor, resulting in a slight decrease in joint hardness at the LHZ. A few fine T_1 forms in the HAZ, and σ develops in the TMAZ. T_1 and S' nucleation is determined by dislocations within the NZ. The LHZ exhibits enhanced precipitation levels, generating coarse T_1 and GBPs, with σ and PFZ.
- (2) Post-weld artificial aging can promote many T_1 formations in the Joints-AA, enhancing joint strength and hardness. Due to varying precipitation ability, the content and size of T_1 in different zones of the joint are inconsistent, resulting in a hardness distribution transforming from a low-amplitude wave curves to a high-amplitude W-shaped curve. The LHZ displays the smallest precipitation ability, forming T_1 with the minimal density and the largest average size, resulting in minimum hardness increment in this region and limited enhancement of the joint strength. The UTS of the joints reaches 506.5 MPa (an increase of 15.1 %), yet elongation decreases to 3.4 %.
- (3) Pre-rolling deformation enhances dislocation density and LAGBs, promoting the formation of high-density, fine T_1 during artificial aging, increasing joint strength and hardness. Pre-deformation especially improves precipitation ability of the LHZ, leading to increased hardness increment after heat treatment, diminishing the hardness disparity between the LHZ and other regions, enhancing uniform deformation ability of the joints with a higher fracture toughness compared to the Joint-AA. The UTS of Joints-R + AA increase to 530.5 MPa (boosting 20.6 %) with a reduced elongation to 3.9 %.

CRediT authorship contribution statement

Peng Chen: Writing – review & editing, Writing – original draft, Methodology, Investigation, Funding acquisition, Data curation, Conceptualization. **Jie Wang:** Writing – review & editing. **Ge Liu:** Investigation. **Wenhao Chen:** Investigation, Data curation. **Yang Tang:** Resources, Methodology. **Bensheng Huang:** Resources, Methodology. **Zhiqing Zhang:** Supervision, Resources, Methodology.

Declaration of competing interest

We would like to submit the enclosed manuscript entitled “Influence of post-weld rolling and artificial aging on microstructure and mechanical properties of friction stir welded 2195-T4 Al-Li alloy joints”, which we wish to be considered for publication in Materials Science & Engineering A.

No conflict of interest exists in the submission of this manuscript, and manuscript is approved by all authors for publication. I would like to declare on behalf of my co-authors that the work described was original research that has not been published previously, and not under consideration for publication elsewhere, in whole or in part. All the authors listed have approved the manuscript that is enclosed.

Data availability

Data will be made available on request.

Acknowledgements

This research is financially supported by Natural Science Foundation in Sichuan Province (2023NSFC0915), Postdoctoral Research Project Special Fund in Sichuan Province, Natural Science Starting Project of SWPU (2023QHZ017), and Project Supported by Scientific and Technological Research Program of Chongqing Municipal Education Commission (KJQN202201436).

Appendix A. Supplementary data

Supplementary data to this article can be found online at <https://doi.org/10.1016/j.msea.2024.147165>.

References

- [1] R.J.H. Wanhill, G.H. Bray, *Aluminum-Lithium Alloys*, Elsevier, Butterworth-Heinemann, Kidlington, 2014, pp. 27–58.
- [2] Y. Yang, J. Bi, H. Liu, Y. Li, M. Li, S. Ao, et al., Research progress on the microstructure and mechanical properties of friction stir welded Al Li alloy joints, *J. Manuf. Process.* 82 (2022) 230–244.
- [3] Z. Yu, J. Qiu, H. Li, P. Cai, L. Zhang, X. Fu, et al., Microstructure, mechanical properties and thermal stability of friction stir processed A-Cu-Mg-Ag alloy, *Mater. Sci. Eng., A* 863 (2023) 144525.
- [4] T. Jiang, T. Jiao, G. Dai, Z. Shen, Y. Guo, Z. Sun, et al., Microstructure evolution and mechanical properties of 2060 Al-Li alloy via friction stir additive manufacturing, *J. Alloys Compd.* 935 (2023) 68019.
- [5] R.J.H. Wanhill, G.H. Bray, Elsevier, Butterworth-Heinemann, 2014, pp. 503–535. Kidlington.
- [6] R. Mishra, H. Sidhar, *Friction Stir Welding of 2xxx Aluminum Alloys Including Al-Li Alloys*, first ed., Elsevier, USA, 2016.
- [7] M.N. Avettand-Fénoël, R. Taillard, J. Laye, T. Odièvre, Experimental investigation of three-dimensional (3-D) material flow pattern in thick dissimilar 2050 friction-stir welds, *Metall. Mater. Trans. A* 45 (2013) 563–578.
- [8] Y. Hovanski, J.E. Carsley, K.D. Clarke, P.E. Krajewski, Friction-stir welding and processing, *JOM (J. Occup. Med.)* 67 (2015) 996–997.
- [9] Attallah MM, Salem HG, Friction stir welding parameters: a tool for controlling abnormal grain growth during subsequent heat treatment, *Mater. Sci. Eng., A* 20053;91:51–59.
- [10] H.S. Lee, J.H. Yoon, J.T. Yoo, K. No, Friction stir welding process of aluminum-lithium alloy 2195, *Process Eng.* 149 (2016) 62–66.
- [11] J. Zhang, X.S. Feng, J.S. Gao, H. Huang, Z.Q. Ma, L.J. Guo, Effects of welding parameters and post-heat treatment on mechanical properties of friction stir welded AA2195-T8 Al-Li alloy, *J. Mater. Sci. Technol.* 34 (2018) 219–227.
- [12] F.F. Wang, W.Y. Li, J. Shen, Q. Wen, J.F. dos Santos, Improving weld formability by a novel dual-rotation bobbin tool friction stir welding, *J. Mater. Sci. Technol.* 34 (2018) 135–139.
- [13] C. Gu, X. Yang, W. Tang, T. Luo, R. Wang, Softening behavior of stationary shoulder friction stir welded joint for thick-plate Al-Li-Cu alloy, *J. Mater. Res. Technol.* 20 (2022) 3008–3024.
- [14] G. Zhang, C. Wu, J. Gao, Ultrasonic line source and its coupling with the tool induced heat generation and material flow in friction stir welding, *J. Mater. Res. Technol.* 21 (2022) 502–518.
- [15] P. Chen, T.N. Li, X.R. Yin, Y. Tang, G. Liu, S.B. Wang, et al., The precipitate evolution in friction stir welding of 2195-O Al-Li alloy, *J. Mater. Res. Technol.* 24 (2023) 1991–2006.
- [16] H. Sidhar, R.S. Mishra, Aging kinetics of friction stir welded Al-Cu-Li-Mg-Ag and Al-Cu-Li-Mg alloys, *Mater. Des.* 110 (2016) 60–71.
- [17] A.K. Shukla, W.A. Baeslack, Study of microstructural evolution in friction-stir welded thin-sheet Al-Cu-Li alloy using transmission-electron microscopy, *Scripta Mater.* 56 (2007) 513–516.
- [18] A.K. Shukla, W.A. Baeslack, Study of process/structure/property relationships in friction stir welded thin sheet Al-Cu-Li alloy, *Sci. Technol. Weld. Join.* 14 (2013) 376–387.
- [19] R. Fonda, J.F. Bingert, Precipitation and grain refinement in a 2195 Al friction stir weld, *Metall. Mater. Trans. A* 37 (2006) 3593–3604.
- [20] Z. Shen, S. Chen, L. Cui, D. Li, X. Liu, W. Hou, et al., Local microstructure evolution and mechanical performance of friction stir additive manufactured 2195 Al-Li alloy, *Mater. Char.* 186 (2022) 111808.
- [21] P. Chen, J. Chen, S.Y. Qin, S.Q. Zou, S.B. Song, T. Jiang, et al., Friction stir welding joints of 2195-T8 Al-Li alloys: correlation of temperature evolution, microstructure and mechanical properties, *Mater. Sci. Eng., A* 823 (2021) 141501.
- [22] P. Chen, S.Q. Zou, J. Chen, S.Y. Qin, Q.B. Yang, Z.Q. Zhang, Z.H. Jia, et al., Effect of rotation speed on microstructure evolution and mechanical properties of nugget zone in 2195-T8 Al-Li alloy friction stir welding joints, *Mater. Char.* 176 (2021) 111079.
- [23] Y. Tao, Z. Zhang, B.H. Yu, P. Xue, D.R. Ni, B.L. Xiao, et al., Friction stir welding of 2060-T8 Al Li alloy. Part I: microstructure evolution mechanism and mechanical properties, *Mater. Char.* 168 (2020) 110524.
- [24] H. Chen, L. Fu, P. Liang, Microstructure, texture and mechanical properties of friction stir welded butt joints of 2A97 Al Li alloy ultra-thin sheets, *J. Alloys Compd.* 692 (2017) 155–169.
- [25] A. Malikov, A. Orishich, N. Bulina, E. Karpov, M. Sharafutdinov, Effect of post heat treatment on the phase composition and strength of laser welded joints of an Al-Mg-Li alloy, *Mater. Sci. Eng., A* 765 (2019) 138302.
- [26] A. Malikov, I. Vitoshin, A. Filippov, E. Karpov, K. Kuper, Effect of post-weld heat treatment on the microstructure, phase composition and mechanical properties of dissimilar Al-Mg-Li/Al-Cu-Li laser welded joints, *Opt Laser. Technol.* 173 (2024) 110534.
- [27] J.Q. Sun, Y. Ma, C. Gao, H.Y. Luo, Comprehensive tensile properties improved by deep cryogenic treatment prior to aging in friction-stir-welded 2198 Al-Li alloy, *Rare Met.* 4 (2019).
- [28] I. Vysotskiy, S. Malopheyev, S. Mironov, R. Kaibyshev, Effect of pre-strain path on suppression of abnormal grain growth in friction-stir welded 6061 aluminum alloy, *Mater. Sci. Eng., A* 760 (2019) 206–213.
- [29] X. Xu, X. Ma, G. Zhao, X. Chen, Y. Wang, Abnormal grain growth of 2196 Al-Cu-Li alloy weld seams during extrusion and heat treatment, *J. Alloys Compd.* 867 (2021) 159043.
- [30] M.B. Lezaack, A. Simar, Avoiding abnormal grain growth in thick 7xxx aluminium alloy friction stir welds during T6 post heat treatments, *Mater. Sci. Eng., A* 807 (2021) 140901.
- [31] A. Kalinenko, I. Vysotskii, S. Malopheyev, S. Mironov, R. Kaibyshev, Relationship between welding conditions, abnormal grain growth and mechanical performance in friction-stir welded 6061-T6 aluminum alloy, *Mater. Sci. Eng., A* 817 (2021) 141409.
- [32] A. Kalinenko, I. Vysotskiy, S. Malopheyev, M. Gazizov, S. Mironov, R. Kaibyshev, Suppression of abnormal grain growth in friction-stir welded aluminum by pre-strain rolling: limitation of the approach, *Mater. Sci. Eng., A* 832 (2022) 142388.
- [33] X. Guo, S.H. Wen, H.J. Jiao, S.J. Wu, Effect of aging treatment on microstructure and mechanical properties of TIG welded joints of 2195-T8 Al-Li alloy, *Mater. Char.* 196 (2023) 112576.
- [34] Y.C. Chen, H.J. Liu, J.C. Feng, Effect of post-weld heat treatment on the mechanical properties of 2219-O friction stir welded joints, *J. Mater. Sci.* 41 (1) (2006) 297–299.
- [35] H. Sidhar, R.S. Mishra, A.P. Reynolds, J.A. Baumann, Impact of thermal management on post weld heat treatment efficacy in friction stir welded 2050-T3 alloy, *J. Alloys Compd.* 722 (2017) 330–338.
- [36] D.Y. Liu, Y.L. Ma, J.F. Li, C. Liu, Y. Du, Y.L. Chen, et al., Quench sensitivity and microstructure evolution of the 2060 Al-Cu-Li alloy with a low Mg content, *Mater. Char.* 177 (2021) 111156.
- [37] B. Cai, Z.Q. Zheng, D.Q. He, S.C. Li, H.P. Li, Friction stir weld of 2060 A-Cu-Li alloy: microstructure and mechanical properties, *J. Alloys Compd.* 649 (2015) 19–27.
- [38] Y. Zhou, H. Xiong, Y. Zhang, C. Kong, H. Yu, Microstructure and mechanical properties of AA2024 sheets joined by underwater friction stir welding, *Mater. Char.* 198 (2013) 112749.
- [39] D. Li, H. Liu, S. Du, X. Li, Y. Gao, Y. Zuo, Investigation on material flow and microstructural evolution mechanism in non-thinning and penetrating friction stir welded Al-Cu aluminum alloy, *Mater. Sci. Eng., A* 864 (2023) 144572.
- [40] X.H. Zeng, P. Xue, D. Wang, D.R. Ni, B.L. Xiao, K.S. Wang, et al., Material flow and void defect formation in friction stir welding of aluminum alloys, *Sci. Technol. Weld. Join.* 4 (2018) 1–10.
- [41] J.H. Kim, J.H. Jeun, H.J. Chun, Y.R. Lee, J.T. Yoo, J.H. Yoon, et al., Effect of precipitates on mechanical properties of AA2195, *J. Alloys Compd.* 669 (2016) 187–198.
- [42] Z.Y. Ma, A.H. Feng, D.L. Chen, J. Shen, Recent advances in friction stir welding/processing of aluminum alloys: microstructural evolution and mechanical properties, *Crit Rev Solid State* 43 (2017) 269–333.
- [43] Y. Ni, Y. Liu, P. Zhang, J. Huang, X. Yu, Thermal cycles, microstructures and mechanical properties of AA7075-T6 ultrathin sheet joints produced by high speed friction stir welding, *Mater. Char.* 187 (2022) 111873.
- [44] J. Kang, M. Si, J. Wang, L. Zhou, X. Jiao, A. Wu, Effect of friction stir repair welding on microstructure and corrosion properties of 2219-T8 Al alloy joints, *Mater. Char.* 196 (2023) 112634.

- [45] L. Shi, X. Dai, C. Tian, C. Wu, Effect of splat cooling on microstructures and mechanical properties of friction stir welded 2195 Al-Li alloy, *Mater. Sci. Eng., A* 858 (2022) 144169.
- [46] Z. Yan, D. Wang, X. He, W. Wang, H. Zhang, P. Dong, et al., Deformation behaviors and cyclic strength assessment of AZ31B magnesium alloy based on steady ratcheting effect, *Mater. Sci. Eng., A* 723 (2018) 212–220.
- [47] Z. Zribi, H.H. Ktari, F. Herbst, V. Optasanu, N. Njah, X.R.D. Ebsd, SRS characterization of a casting Al-7wt%Si alloy processed by equal channel angular extrusion: dislocation density evaluation, *Mater. Char.* 153 (2019) 190–198.
- [48] H. Gao, Y.Y. Huang, W.D. Nix, J.W. Hutchinson, Mechanism-based strain gradient plasticity-I. theory, *J. Mech. Phys. Solid.* 47 (6) (2019) 1239–1263.
- [49] L.P. Kubin, A. Mortensen, Geometrically necessary dislocations and strain-gradient plasticity: a few critical issues, *Scripta Mater.* 48 (2) (2003) 119–125.
- [50] V. Araullo-Peters, B. Gault, F. Geuser, A. Deschamps, J.M. Cairney, Microstructural evolution during ageing of Al-Cu-Li-x alloys, *Acta Mater.* 66 (2014) 199–208.
- [51] R. Goswami, N. Bernstein, Effect of interfaces of grain boundary Al_2CuLi plates on fracture behavior of Al-3Cu-2Li, *Acta Mater.* 87 (2015) 399–410.
- [52] B. Malard, F. De Geuser, A. Deschamps, Microstructure distribution in an AA2050 T34 friction stir weld and its evolution during post-welding heat treatment, *Acta Mater.* 101 (2015) 90–100.
- [53] Y.L. Ma, J.F. Li, R.Z. Zhang, J.J. Tang, C. Huang, H.Y. Li, et al., Strength and structure variation of 2195 Al-Li alloy caused by different deformation processes of hot extrusion and cold-rolling, *T Nonferr Metal Soc* 30 (4) (2020) 835–849.
- [54] P. Chen, W.H. Chen, J.X. Chen, Z.Y. Chen, R.X. Yin, Y. Tang, et al., Effect of base material temper condition on precipitate evolution and mechanical properties of 2195 Al Li alloy friction stir welding joints, *Mater. Char.* 209 (2024) 113712.
- [55] Y.Q. Mao, L.M. Ke, F.C. Liu, C.P. Huang, Y. Chen, Q. Liu, Effect of welding parameters on microstructure and mechanical properties of friction stir welded joints of 2060 aluminum lithium alloy, *Int. J. Adv. Manuf. Technol.* 81 (5–8) (2015) 1419–1431.
- [56] J.F. Li, Y.L. Chen, X.H. Zhang, Z. Zq, Structure and mechanical property of friction-stir weld joint of 2195-T8 Al-Li alloy plate, *Rare Met. Mater. Eng.* 47 (3) (2018) 780–787.
- [57] M. Dhondt, I. Aubert, N. Saintier, J.M. Olive, Mechanical behavior of periodical microstructure induced by friction stir welding on Al-Cu-Li 2050 alloy, *Mater. Sci. Eng., A* 644 (2015) 69–75.
- [58] B. Anandan, M. Manikandan, Machine learning approach with various regression models for predicting the ultimate tensile strength of the friction stir welded AA 2050-T8 joints by the K-fold cross-validation method, *Mater. Today Commun.* 34 (2023) 105286.
- [59] S. Kumar, D. Sethi, S. Choudhury, B. Saha Roy, S.C. Saha, An experimental investigation to the influence of traverse speed on microstructure and mechanical properties of friction stir welded AA2050-T84 Al-Cu-Li alloy plates, *Mater. Today: Proc.* 26 (2020) 2062–2068.
- [60] H. Liu, Y. Hu, C. Dou, D.P. Sekulic, An effect of the rotation speed on microstructure and mechanical properties of the friction stir welded 2060-T8 Al-Li alloy, *Mater. Char.* 123 (2017) 9–19.
- [61] K. Yan, T.Y. Wang, H. Liang, Y. Zhao, Effects of rotation speed on microstructure and mechanical properties of 2060 Al-Cu-Li alloy in friction stir welding, *J. Mater. Eng. Perform.* 27 (11) (2018) 5803–5814.
- [62] A.R. Cisko, J.B. Jordon, R.L. Amaro, P.G. Allison, J.S. Wlodarski, Z.B. McClelland, et al., A parametric investigation on friction stir welding of Al-Li 2099, *Mater. Manuf. Process.* 35 (10) (2020) 1069–1076.
- [63] C. Bitondo, U. Prisco, A. Squilace, P. Buonadonna, G. Dionoro, Friction-stir welding of AA 2198 butt joints: mechanical characterization of the process and of the welds through DOE analysis, *Int. J. Adv. Manuf. Technol.* 53 (5–8) (2011) 505–516.
- [64] Y. Tao, Z. Zhang, P. Xue, D.R. Ni, B.L. Xiao, Z.Y. Ma, Effect of post weld artificial aging and water cooling on microstructure and mechanical properties of friction stir welded 2198-T8 Al-Li joints, *J. Mater. Sci. Technol.* 123 (2022) 92–112.
- [65] Y. Chen, H. Ding, J.Z. Li, J.W. Zhao, M.J. Fu, X.H. Li, Effect of welding heat input and post-welded heat treatment on hardness of stir zone for friction stir-welded 2024-T3 aluminum alloy, *T Nonferr Metal Soc* 25 (8) (2015) 2524–2532.
- [66] G.D. Sun, L. Zhou, Y.N. Liu, H.F. Yang, J.T. Jiang, G.A. Li, Microstructure characterization and evaluation of mechanical properties in 2A97 aluminum-lithium alloys welded by stationary shoulder friction stir welding, *J. Mater. Res. Technol.* 16 (2022) 416–432.
- [67] E. Lertora, C. Gambaro, AA8090 Al-Li alloy FSW parameters to minimize defects and increase fatigue life, *Int. J. Material Form.* 3 (2010) 1003–1006.
- [68] S.Y. Shivryari, A.H. Monazzah, Study on the balance between FSW parameters and heat treatment for an optimized Al2024-T8 joint: microstructural and tensile evaluations, *Prod. Eng.* 15 (5) (2021) 595–603.
- [69] I.S. Zuiko, S. Mironov, S. Betsofen, R. Kaibyshev, Suppression of abnormal grain growth in friction-stir welded Al-Cu-Mg alloy by lowering of welding temperature, *Scripta Mater.* 196 (2021) 113765.

Further reading

- [1] N. Nayan, M. Yadava, R. Sarkar, S.V.S.N. Murty, N.P. Gurao, S. Mahesh, et al., Microstructure and tensile response of friction stir welded Al-Cu-Li (AA2198-T8) alloy, *Mater. Char.* 159 (2020) 110002.
- [2] C. Liu, Z. Ma, P. Ma, L. Zhan, M. Huang, Multiple precipitation reactions and formation of θ' -phase in a pre-deformed Al-Cu alloy, *Mater. Sci. Eng., A* 733 (2018) 28–38.
- [3] L. Zhou, C.L. Wu, P. Xie, F.J. Niu, W.Q. Ming, K. Du, et al., A hidden precipitation scenario of the θ' -phase in Al-Cu alloys, *J. Mater. Sci. Technol.* 75 (2021) 126–138.